

eISSN 2657-7291

2020 (LXI)  
Vol. 220/221, No. 1-2

# SCIENTIFIC JOURNAL OF POLISH NAVAL ACADEMY

Formerly ZESZYTY NAUKOWE AKADEMII MARYNARKI WOJENNEJ



Gdynia 2020

## SCIENTIFIC BOARD

Rear Adm. Tomasz Szubrycht, Prof. (Chairman), Polish Naval Academy, Poland  
Rear Adm. Vergil Chitac, Prof. PhD, Naval Academy, 'Mircea cel Batran', Romania  
Franciszek Grabski, Prof., Polish Naval Academy, Poland  
Capt (N) Kalin Kalinov, Prof. PhD, Nikola Vaptsarov Naval Academy, Bulgaria  
Gvidonas Labeckas, Prof., Aleksandras Stulginskis University, Litwa  
Commodore Boyan Mednikarov, Prof. DSc, Nikola Vaptsarov Naval, Bulgaria  
Jerzy Merkisz, Prof., Poznan University of Technology, Poland  
Suleyman Ozkaynak, Prof., Piri Reis University, Turkey  
Rear Adm. Juan L. Sobrino Pérez-Crespo, Spain  
Takeshi Shinoda, Prof., Kyushu University, Japan

## EDITORIAL COMMITTEE

Editor-in-Chief  
Zygmunt Kitowski, Prof.

Managing Editor, Executive Editor  
Beata Róžańska, MSc

Associate Editors  
Andrzej Grządziela, Ass. Prof. (*Mechanical Engineering*)  
Jerzy Garus, Ass. Prof. (*Automatic Control, Electronics  
and Electrical Engineering*)  
Andrzej Felski, Prof. (*Civil Engineering and Transportation*)  
Ryszard Studański, PhD Eng. (*Technical Computer Sciences  
and Telecommunications*)

Language Editors  
James Marson, MSc, Eng.  
Beata Róžańska, MSc

Statistical Editor  
Agata Załęska-Fornal, PhD Eng.

All articles in the quarterly have been peer reviewed  
The original (reference) version of the journal is the online version

## Abstracting & Indexing

Arianta  
Baidu Scholar  
BazTech  
CEON Biblioteka Nauki  
CNKI Scholar (China National Knowledge  
Infrastructure)  
CNPIEC  
Dimensions  
EBSCO Discovery Service  
Google Scholar

Index Copernicus  
J-Gate  
KESLI-NDSL (Korean National Discovery for Science Leaders)  
Naviga (Softweco)  
POL-index  
Primo Central (ExLibris)  
ReadCube  
Summon (Serials Solutions/ProQuest)  
TDNet  
WorldCat (OCLC)

## Website quarterly

<https://content.sciendo.com/view/journals/sjpna/sjpna-overview.xml>

<https://www.amw.gdynia.pl/index.php/nauka/czasopisma-naukowe/item/45-zeszyty-naukowe>

## Journal Owner and Publisher

Akademia Marynarki Wojennej/Polish Naval Academy

## Contact

Redakcja Zeszytów Naukowych AMW  
Akademia Marynarki Wojennej  
Inż. J. Śmidowicza 69, 81-127 Gdynia  
tel. 261 26 29 72  
e-mail: b.rozanska@amw.gdynia.pl

## CONTENTS

**Stanisław Hożyń, Marcin Przybysz**

Detection of unmanned aerial vehicles using computer vision methods:  
a comparative analysis ..... 5

**Radosław Kiciński, Wojciech Jurczak**

Mechanical properties of welded joints of 1.3964 steel for Computer Aided Engineering  
(CAE) purposes ..... 15

**Karolina Zwolak, Łukasz Marchel, Marcin Skóra, Radosław Przybysz,  
Rafał Józwiak, Kinga Tomaszewska**

Accessibility and usability of Landsat 8 data for the purpose of satellite-driven  
bathymetry of the South Baltic near-shore waters on the example of Gulf of Gdańsk.... 29

**Artur Bogdanowicz, Marcin Zacharewicz, Jakub Król**

The use of a microcontrollers in hygrometric measurements application..... 47

**Rafał Warżała**

Modern integrated platform management system laboratory for Polish Naval Academy:  
design and implementation..... 59

**Michał Brodzicki, Przemysław Chrabąszcz**

A concept of BLDC drive model containing battery cell model ..... 73





## DETECTION OF UNMANNED AERIAL VEHICLES USING COMPUTER VISION METHODS: A COMPARATIVE ANALYSIS

Stanisław Hożyń\*<sup></sup>, Marcin Przybysz\*\*<sup></sup>

\* *Polish Naval Academy, Faculty of Mechanical and Electrical Engineering, Śmidowicza 69 Str., 81-127 Gdynia, Poland; e-mail: s.hozyn@amw.gdynia.pl; ORCID ID: 0000-0003-1422-0330*

\*\* *Polish Naval Academy, Faculty of Navigation and Naval Weapons, Śmidowicza 69 Str., 81-127 Gdynia, Poland; e-mail: przyprzy@gmail.com; ORCID ID: 0000-0002-4243-4566*

### ABSTRACT

Detection of small objects in the airspace is a crucial task in the military. In the era of today's unmanned aerial vehicles (UAVs) technology, many military units are exposed to recognition and observation through flying objects. They are often equipped with optoelectronic warhead making a way to collect essential and secret data of the military unit. Modern technical solutions make it possible to implement some methods facilitating detection of flying objects. A lot of them utilize computer vision techniques based on image processing algorithm. Therefore, in this article, we present an analysis of the most promising algorithm for detection of small flying objects.

#### Keywords:

unmanned aerial vehicle (UAVs), computer vision, object detection.

#### Research article

© 2020 Stanisław Hożyń, Marcin Przybysz  
This is an open access article licensed under the Creative Commons  
Attribution-NonCommercial-NoDerivatives 4.0 license  
(<http://creativecommons.org/licenses/by-nc-nd/4.0/>)

## INTRODUCTION

Unmanned aerial vehicles (UAVs) constitutes severe danger to military units. Therefore, many systems devoted to detecting small flying objects have been developed. Some of them are based on time measurement of the electromagnetic field emitted by the UAVs. Range of these techniques depends on the transmitter power; however, the characteristics of the measurement location also affect the detection results. Therefore, to improve the detection efficiency, the set of many 3D antennas, set in an omnidirectional manner, are in effect.

The radar station is a device that has been used for object detection in the air-space in both civil and military aviation. The main task of radar is to scan the space to detect threats such as enemy rockets, aeroplanes or UAVs. Such a system works on the principle of emitting electromagnetic waves. After reaching the object, the waves are reflected and return to the receiver. In this process, the object's speed and location are determined [11].

Another approach utilises radar systems, where that radio beams or microwave waves reflect from materials such as metals and carbon fibres are analysed. By using stable frequency generators and high accuracy time measurement systems, the position and velocity of an object can be determined with high precision. An operating range of a radar amounts to 500 km; however, it increases when radars are connected into a network. Effectiveness of such systems depends on the size of a reflection surface of the object, so detecting small object at a large distance from the radar could be difficult. For that reason, the American army has conducted detection of small objects tests with AN/TPQ 49 radar, used under standard conditions to detect artillery fire. This radar has been recognized as highly reliable in open space; however, its reliability was reduced in airport areas due to electromagnetic noise.

Some techniques apply an acoustic system, utilizes specific sound emitted by objects to detect the direction of the emission [3]. This system does not require tracking of an unidentified flying object and works under various weather conditions all hours of the day and night. To perform, it uses acoustic arrays consisting of highly sensitive microphones. By using a large number of them (usually about 128) and advanced digital signal processing, the system enables azimuth and elevation determination of the target in real-time.

Mixed systems using a radar sensor, acoustic matrix and video cameras are mainly used to detect drones. However, thanks to the implementation of multiple

sensors, they can be used to recognise other air and ground dangers. The most important sensor is radar, supported by the acoustic matrix and video cameras. This combination of three sensors allows detection of small drones up to 1000 meters. After revealing the object's invasion into the protected space, the software visualizes the entire event and archives it through recording of radar and video signal. The system also makes it possible to detect enemy objects by their sounds; however, to do this, it needs a sound signature of the object.

Computer vision systems have received attention recently due to their convenient application for small object detection [10]. This results from the increasing availability of optical sensors and a large number of image processing algorithms. In essence, the majority of algorithms are based on fundamental image processing techniques such as image segmentation, optical flow and background subtraction. Some methods utilise artificial intelligence to detect, recognize and classify objects [7]. This solution was introduced by IntelliVIX company for the task of object detection. The system works in combination with artificial intelligence that allows not only to detect a given object but also classify it using on previously learned cases. It also can recognize a predefined event and register new objects in the database.

Since computer vision plays an essential role in small object detection, the comparative analysis of image processing algorithms was conducted in this study. First, the compared algorithms are described. Then, the results of the experiments are presented, and, finally, the conclusions are formulated.

## **METHODS**

In our research, we focused on detecting AUVs using a vision system. For this purpose, we implemented computer vision methods described below.

### **Classifiers learning with supervision**

This object detection technique uses learning methods to recognize objects automatically. In this approach, the classifier employs initially prepared patterns to create learning mapping functions. It solves the classification problem, especially when the algorithm approximates the behaviour of a function by generating results in the form of either discrete labels or continuous values. Learning patterns have both pairs of object features and properties labels that are specified manually. Having a previously defined database, it builds a model (e.g. logical rules, decision trees) to

classify new objects or update existing division of objects in the predefined classes [1]. This process consists of several stages: model building, testing phase and prediction of unknown values. To build a formal model, the classifier is used as input data consisting of examples, observations and samples [2]. The most popular algorithmic implementations of this technique are KNN, Codebook and Codebook2.

### **Background subtraction**

Background subtraction is a process of determining the foreground object while maintaining the background model. The foreground object can be any object that has been detected as a difference sequence frame with the background model. Such a result can be further used to track targets or detect motion [9]. The term background is not strictly described because it differs depending on the considered case. The most common part of the background is the part of the scene that is static, or which shows little change for a limited time. A dynamic background model is one in which the background scenes may contain moving elements in an external environment, for example, moving grass in the wind. In the construction of a static representation of the scene, non-parametric statistical modelling of pixel process is used [6]. Background subtraction is a widely used approach for detecting moving objects using a static camera. The main reason for using this method is its simple structure and accuracy. This method, to be able to cope with changing environmental conditions, demands properly selected parameters [8]. In general, it involves detecting differences between the model and subsequent image frames. The result of this operation creates a binary mask that includes pixels of moving objects. At the same time, the pixels belonging to the part of the object are grouped together [5]. Any system that is devoted to detecting objects has to be able to distinguish between these two areas [4]. The modifications of background subtraction were implemented in MOG, MOG2 and GMG algorithms.

## **RESULTS**

This section presents the results of research on the use of seven algorithmic implementations of methods mentioned above: Background Subtraction, MOG, MOG2, GMG, KNN, Codebook and Codebook2. The algorithms have been tested for computational complexity, accuracy, detection time, amount of noise and a number of lost objects. To perform tests, the algorithms were designed and implemented using

the C++ language and the OpenCV library. The experiments were carried out using ten videos, presenting small and medium-size UAVs moving at different distances from the camera and under various weather conditions. The exemplary frame from one of the analysed movies is presented in fig. 1.



Fig. 1. Example of the image used during the experiment

The number of lost objects constitutes a crucial parameter for the correct execution of the algorithms because it increases the risk of invading the protected area. The statistics for the analysed methods are presented in fig. 2.

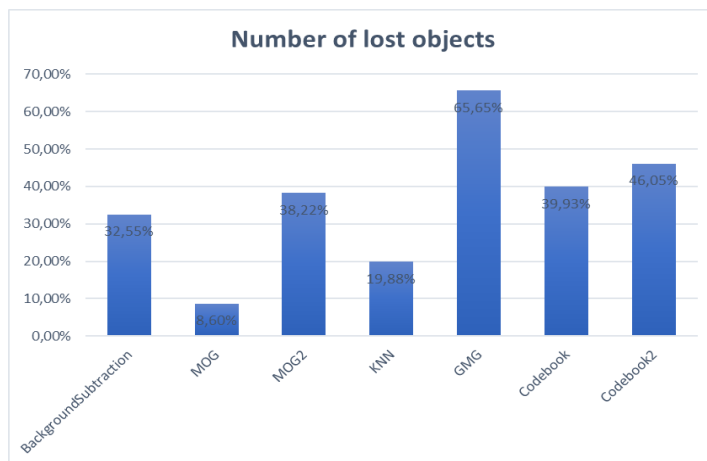


Fig. 2. Number of lost objects

The GMG algorithm yields the least efficiency among the analysed methods, which leads to more frequent loses the detected object. In contrast, the MOG algorithm gives the best results; as a result, it practically does not lose the detected object.

Computational complexity was analysed using the time needed for a given algorithm to perform a single loop of the entire calculation process. The longest time was considered as a reference point, and the remaining algorithms were compared to it. The results are presented in the figure below.

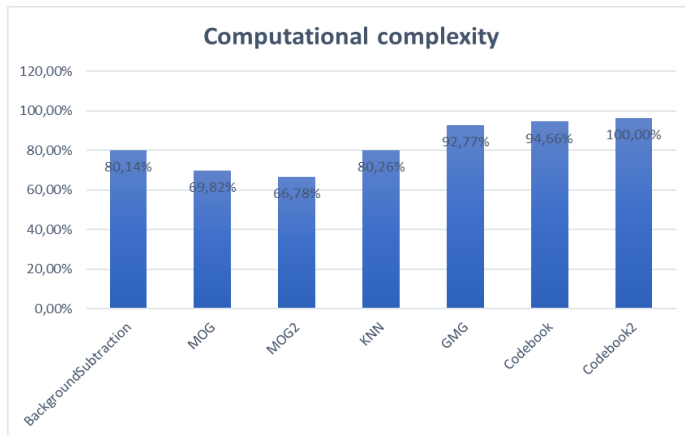


Fig. 3. Computational complexity of the tested algorithms

The detection time was counted from the beginning of image acquisition to the detection of the object. The obtained results were compared to the longest time and presented in fig. 4.

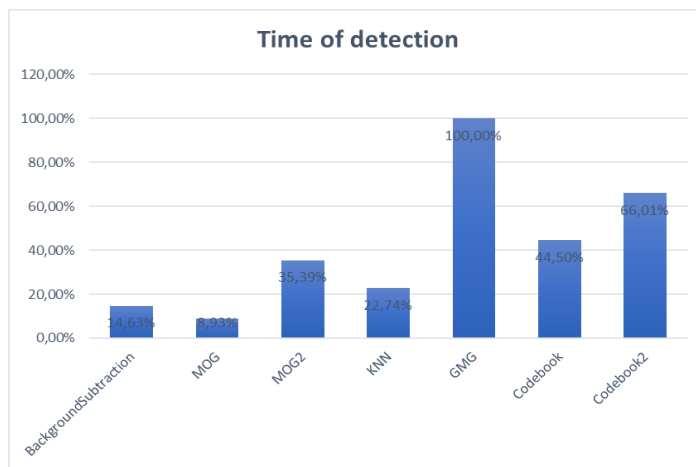


Fig. 4. Time of detection

Among the analysed algorithms, the MOG was characterised by the shorter detection time. Relatively short detection time was observed using the Background

Subtraction and KNN algorithms. Detection time of GMG, Codebook and Codebook2 algorithms was longer due to the learning process performed at initial steps.

The amount of noise was determined by an area of small objects erroneously detected in the image. To estimate it, the image was divided into square areas, as shown in fig. 5. Then, the ratio of squares containing noise to the whole number of squares in the image was calculated.

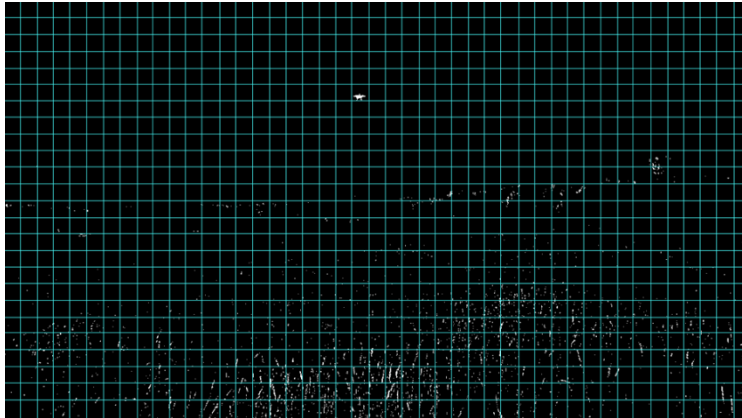


Fig. 5. Example of noise calculation

The obtained results indicate that the Background subtraction, MOG and MOG2 algorithms generate a low level of noise. Conversely, the Codebook and Codebook2 algorithms generate the highest but acceptable level of noise. The results are depicted in fig. 6.

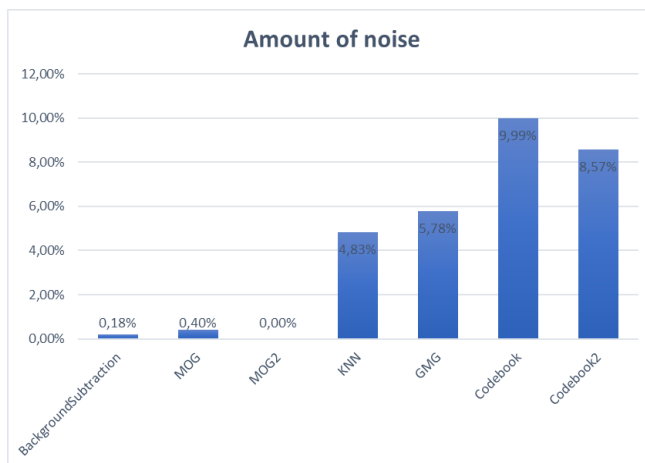


Fig. 6. Amount of noise

The accuracy of drone detection represents the percentage of correctly classified drone pixels as the foreground. Fig. 7 shows the obtained results.

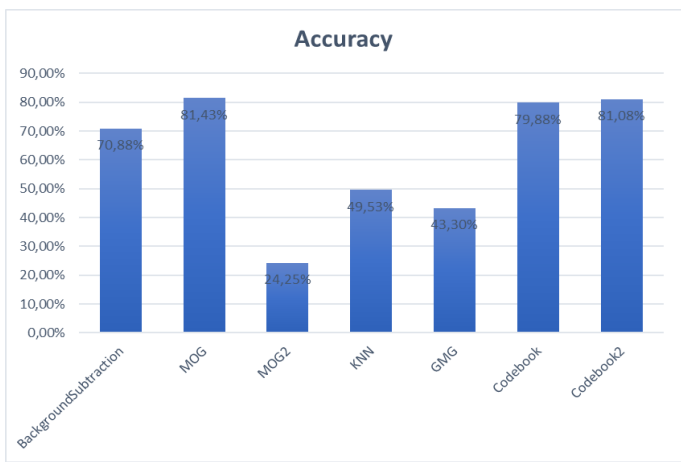


Fig. 7. Accuracy of drone detection

The best performance is demonstrated by the MOG, Codebook and Codebook2 techniques. The Background Subtraction yields only slightly worse results.

### SUMMARY

The analysis showed that the MOG algorithm outperforms other methods in most statistics. Comparing with others, it demonstrated high performance in terms of calculations and memory requirements ensuring effective noise removal in the images. What is more, it can detect the object after comparing two consecutive frames, which makes it highly effective. Its most significant advantage is that it detects the object and prevent its disappearance with remarkably high accuracy.

### REFERENCES

- [1] Baggio D. et al., *Mastering OpenCV with Practical Computer Vision Projects*, Packt Publishing Ltd., Birmingham 2012.
- [2] Bradski G., Kaehler A., *Learning OpenCV*, O'Reilly Media, Inc., Sebastopol 2008.
- [3] Busset J. et al., *Detection and tracking of drones using advanced acoustic cameras*, Proc. SPIE, Conference Paper, 2015, pp. 21–33, DOI: 10.1117/12.2194309.
- [4] Cheung S. S., Kamath C., *Robust techniques for background subtraction in urban traffic video*, 'EURASIP J. Adv. Signal Process', 2005, pp. 88–101, DOI: 10.1155/ASP.2005.2330.

- [5] Elhabian S. Y., El-Sayed K. M., Ahmed S. H., *Moving Object Detection in Spatial Domain using Background Removal Techniques — State-of-Art*, 'Recent Patents on Computer Science', 2010, Vol. 1, No. 1, pp. 32–54, DOI: 10.2174/2213275910801010032.
- [6] Hożyń S., Żak B., *Distance Measurement Using a Stereo Vision System*, 'Solid State Phenomena', 2013, Vol. 196, pp. 189–197, DOI: 10.4028/www.scientific.net/SSP.196.189.
- [7] Hożyń S., Żak B., *Local image features matching for real-time seabed tracking applications*, 'Journal of Marine Engineering and Technology', 2017, Vol. 16, No. 4, pp. 273–282, DOI: 10.1080/20464177.2017.1386266.
- [8] Hożyń S., Żak B., *Moving Object Detection, Localization and Tracking Using Stereo Vision System*, 'Solid State Phenomena', 2015, Vol. 236, pp. 134–141, DOI: 10.1007/978-3-319-10990-9\_39.
- [9] Li Y., Wang S., Tian Q., Ding, X., *A survey of recent advances in visual feature detection*, 'Neuro-computing', 2014, Vol. 149, pp. 736–751, DOI: 10.1016/j.neucom.2014.08.003.
- [10] Szeliski R., *Computer Vision: Algorithms and Applications*, Vol. 5. London: Springer-Verlag, London 2011, eBook ISBN 978-1-84882-935-0, DOI: 10.1007/978-1-84882-935-0.
- [11] Yoon J. H., Xu H., Garcia Carrillo L. R., *Advanced Doppler radar physiological sensing technique for drone detection*, Proceedings of SPIE — The International Society for Optical Engineering, 2017, Vol. 10188, pp. 10–21, DOI: <https://doi.org/10.1117/12.2262758>.

## **ANALIZA METOD WYKRYWANIA BEZZAŁOGOWYCH STATKÓW POWIETRZNYCH WYKORZYSTUJĄCYCH TECHNIKI WIDZENIA KOMPUTEROWEGO**

### **STRESZCZENIE**

W artykule przedstawiono analizę metod wykrywania bezzałogowych statków powietrznych wykorzystujących techniki widzenia komputerowego.

Słowa kluczowe:

bezzałogowy statek powietrzny, widzenie komputerowe, wykrywanie obiektów.

---

*Article history*

Received: 30.03.2020

Reviewed: 16.04.2020

Revised: 19.04.2020

Accepted: 27.04.2020





## MECHANICAL PROPERTIES OF WELDED JOINTS OF 1.3964 STEEL FOR COMPUTER AIDED ENGINEERING (CAE) PURPOSES

Radosław Kiciński<sup>1</sup>, Wojciech Jurczak<sup>2</sup>

*Polish Naval Academy, Faculty of Mechanical and Electrical Engineering, Śmidowicza 69 Str., 81-127 Gdynia, Poland; e-mail: r.kicinski@amw.gdynia.pl, w.jurczak@amw.gdynia.pl; ORCID ID: 10000-0003-3490-1301, 20000-0002-1608-7249*

### ABSTRACT

The article presents the study of mechanical properties of welded steel from which the hull of a modern mine destroyer was made. Keeping the tightness of ship compartments during operation depends on the strength of these joints. The results of testing the mechanical properties of 1.3964 steel and its welded joints subjected to a static tensile test were presented, and a Johnson – Cook material model was proposed. The material model can be used in CAE (Computer Aided Engineering) simulations related to hull strength analysis.

#### Keywords:

Computer Aided Engineering, austenitic steel, true material characteristic, welding.

#### Research article

© 2020 Radosław Kiciński, Wojciech Jurczak  
This is an open access article licensed under the Creative Commons  
Attribution-NonCommercial-NoDerivatives 4.0 license  
(<http://creativecommons.org/licenses/by-nc-nd/4.0/>)

## INTRODUCTION

Operational problems of offshore structures, also made of austenitic stainless steel, are caused not only by the impact of the marine environment causing corrosion, but also by operating conditions associated with the impact of operational stresses. The strength of the load-bearing elements of each structure ensures its operational reliability and operational safety. The marine structure consists of elements that are most often joined as a result of welding. The strength of welded joints depends on many factors, but primarily on the mechanical properties of the welded structural material, the type of binder used, the method and welding parameters.

Austenitic alloys are the most popular stainless steels because of their excellent ability to plastic deformation, corrosion resistance and weldability [1], which is why they are often used in shipbuilding. They are non-magnetic in the annealed condition, which is why they are intended, for example, for the construction of modern mine destroyers. Mine destroyer hulls are built of non-magnetic steel ensuring low characteristics of ship's physical fields.

Prefabrication, assembly of sections, blocks and hull takes place in a special hall equipped with monitoring systems and specialized filtering and controlling devices, including cleanliness and air temperature, as well as preventing iron filings and other external contaminants from entering [4].

In shipbuilding practice, the method of welding austenitic steels is GTAW (Gas Tungsten Arc Welding), also known as the TIG (Tungsten Inert Gas) or WIG (Wolfram Inert Gas) method. The energy necessary to melt the metal is supplied by an electric arc struck and held between the tungsten or tungsten alloy electrode and the welded element in an inert gas atmosphere. Stainless steels are always welded with direct current at negative polarity (DCEN — Direct Current Electrode Negative or DCSP — Direct Current Straight Polarity). Under these conditions, the electron flux hits the welded piece, which increases fusion, while the tungsten oxide (2% ThO<sub>2</sub>) tungsten oxide electrode usually consumes slightly. Welding parameters are voltage, welding current, welding speed and shielding gas flow. If a binder is used, it is either in the form of bare rods or in the form of coils for automatic welding. The inert gas flow, which protects the arc zone from the surrounding air, allows the arc to remain very stable. Depending on the welded material, the shielding gas consists mainly of a mixture of argon (Ar), helium (He) and hydrogen (H<sub>2</sub>) [10]. The correct selection of welding parameters for thermal joining of particular austenitic steel is usually the *know-how* of the contractor, which is obtained during multi-variant trials and tests.

During welding, care should be taken to preserve welding technology, which has a direct impact on the quality of joints.

The 1.3964 non-magnetic steel also designated as EN X2CrNiMoNNb 21-16-5-3 is well weldable and resistant to sea water up to 40°C, as well as intergranular stress corrosion [8]. However, the correct chemical composition of the binder should be chosen to ensure adequate strength and good corrosion resistance. The chemical composition of 1.3964 steel is given in the tab. 1.

Tab. 1. Chemical composition of 1.3964 steel

<i>EN-10088</i>		<b>1.3964/ X2CrNiMoNNb 21-16-5-3</b>	
<i>ASTM XM</i>		<b>19</b>	
<i>Chemical composition</i>		<i>according to the manufacturer [7]</i>	<i>according to the metallurgical certificate</i>
<b>C</b>	%	max 0.03	0.012
<b>Mn</b>	%	4–6	4.42
<b>Cr</b>	%	20–21.5	20.32
<b>Ni</b>	%	15–17	15.46
<b>Mo</b>	%	3–3.5	3.15
<b>Nb</b>	%	max 0.25	0.12
<b>N</b>	%	<0.11	0.305
<b>Fe</b>	%	residue	residue
<b>Si</b>	%	–	0.36
<b>P + S</b>	%	max 0,019 + 0 0004	

Binder recommended by the manufacturer for welding 1.3694 steel is 1.3954 and 1.3984 [6]. For the tests described in this article, samples welded manually and semi-automatically with 1.3954 binder were used.

## MATERIALS AND METHODS

Strength tests were carried out using the MTS 810 machine in accordance with the standard [9]. Properly prepared specimens (fig. 1) were stretched at a rate of 0.12 mm/s. During tests with an interval of 0.2 s, digital images of the sample surface were recorded with contrast applied for the method of digital image correlation (DIC) using images recorded simultaneously by at least two cameras.

Then these images are processed and used to calculate the deformation fields in the vicinity of the place where the original deformation was located. The 3D

method was chosen because of the non-flat surface of the samples due to the presence of welds and in order to avoid the influence of displacements in a direction perpendicular to the surface of the sample, to which the 2D method (using one camera) is sensitive. Before the tests, the system was calibrated based on photos of a calibration grid of known geometry oriented at different angles to the cameras. These photos were used to calculate the relative position of cameras and samples and to scale pixels per mm.

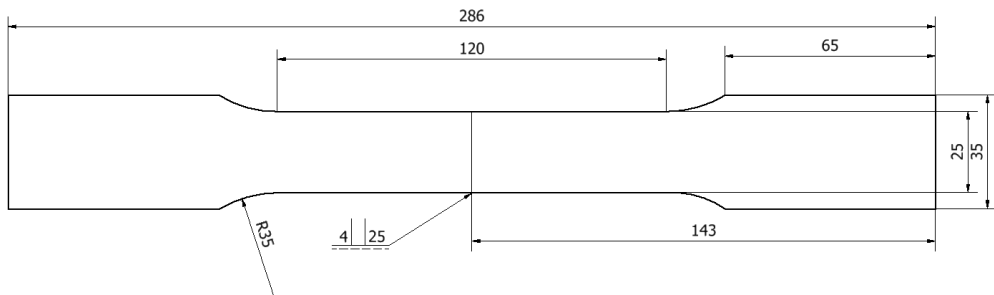


Fig. 1. Specimen dimensions and technical drawing

The measurement of the longitudinal component of the deformation of the area for which the highest values were observed at the final stage of the tests was used to calculate the actual stress in the way presented in [4] as method II. That article showed a high compliance of the method in comparison with a much more complicated method (method I) based on the simultaneous measurement of narrowing of both side surfaces of the sample using 4 cameras. The actual stress was calculated from the formula:

$$\sigma = \frac{F}{A_0} e^{\varepsilon_{xx}} \quad (1)$$

where:

$F$  — force;

$A_0$  — initial cross-sectional area (outside the weld);

$\varepsilon_{xx}$  — longitudinal component of logarithmic strain tensor.

## RESULTS

### Base material

For 1.3964 steel specimens with a rectangular cross-section, the method of taking a sample from a sheet metal along or transversely to the rolling direction has

an effect on strength properties. Based on the engineering stretching curve, real characteristics were developed in accordance with the methodology contained in [11] and presented in fig. 2 and in tab. 2.

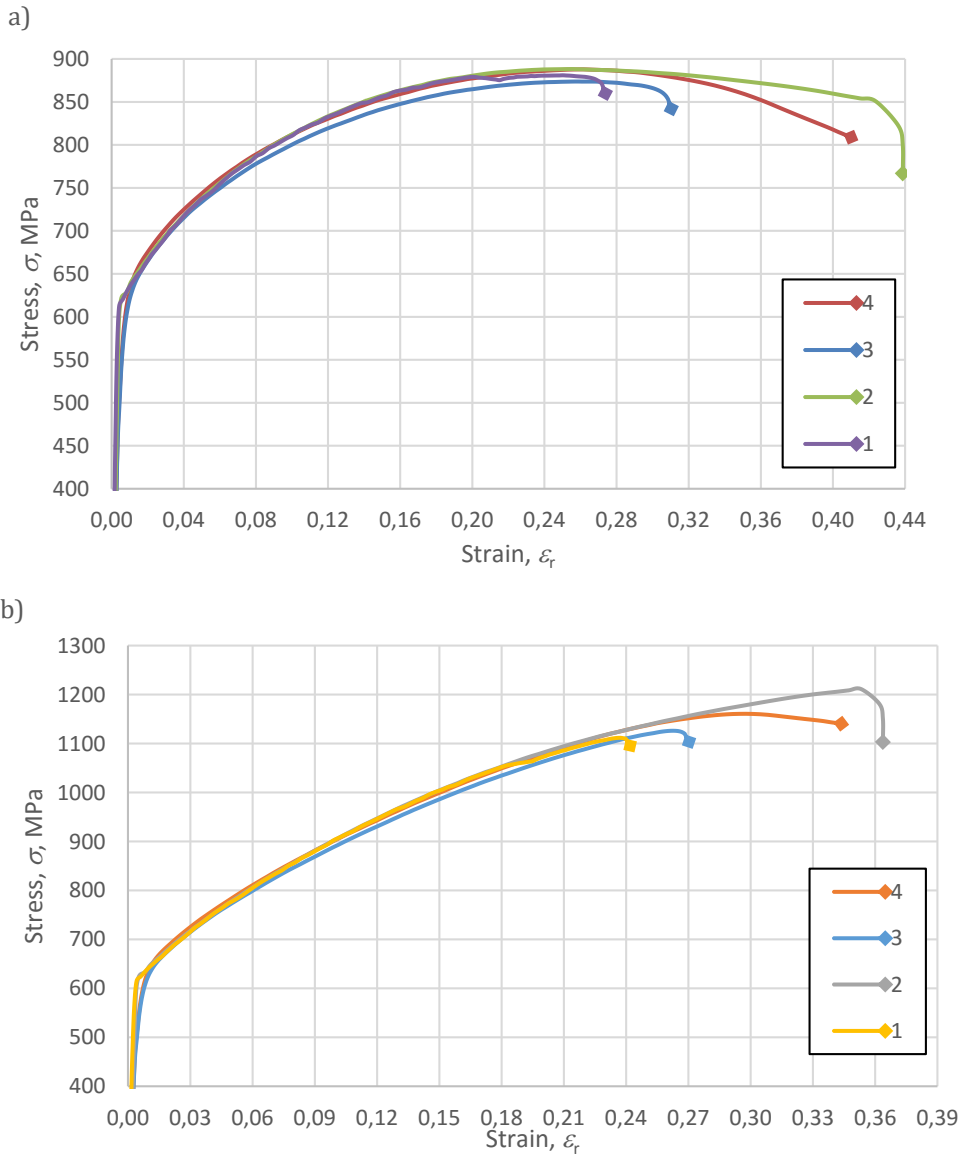


Fig. 2. Selected characteristics of 1.3964 austenitic steel for flat specimens taken along the rolling direction (2 and 4) and perpendicular to the rolling direction (1 and 3): a) nominal, b) true

Tab. 2. Summary of mechanical properties for flat 1.3964 steel samples taken along and perpendicular to the rolling direction

Steel 1.3964	Young modulus	Yield point	Yield strain	Ultimate strength	Ultimate strain
Position to the rolling direction	$E$ , GPa	$R_e$ , MPa	$\epsilon_n$ , -	$R_m$ , MPa	$\epsilon_r$ , -
perpendicularly	221.0	569.6	0.043	1126.4	0.3285
1/perpendicularly		615.1	0.042	1111.7	0.2365
3/perpendicularly		501.3	0.044	1126.0	0.2615
<b>Average</b>		<b>562</b>	<b>0.0042</b>	<b>1121.5</b>	<b>0.2615</b>
along	215.2	533.4	0.0042	1158.1	0.3581
2/along		625.5	0.0054	1211.1	0.3533
4/along		557.7	0.0055	1160.7	0.2945
<b>Average</b>		<b>572.2</b>	<b>0.0048</b>	<b>1176.6</b>	<b>0.3353</b>

Rolling direction has an effect on the plastic properties of 1.3964 base steel material. At a similar strength limit  $R_m = 880 - 900$  MPa for both rolling directions, the deformation was reduced by about 30% for samples taken perpendicular to the rolling direction (fig. 2a). Fig. 2b shows the actual strength characteristics verified by the DIC method, where a change in the nature of the course after exceeding the yield point was noted, resulting from the change in the cross-sectional area of the tested sample. The use of the DIC method illustrates the increase in the strength limit  $R_m$  by 250 MPa for samples taken perpendicular to the rolling direction and by 295 MPa for samples taken along the rolling direction in relation to the nominal characteristics.

Referring to round samples, in tests of rectangular cross-section samples there was less variation in plastic properties (from 30% to 5%) between samples taken along and perpendicular to the rolling direction with a similar increase in material strength [3]. Therefore, for comparative tests for welded joints, nominal and true characteristics were determined, and then the Johnson - Cook (JC) model was proposed in form [2]:

$$\sigma = (A + B\epsilon^n) \quad (2)$$

where:

$\sigma$  — stress;

$A$  — material constant;

$B$  — strengthening parameter;

- $\varepsilon$  — reduced plastic strain;  
 $n$  — exponent of strengthening.

Constants for the model were obtained using the MATLAB environment and a specially prepared calculation program. The JC model obtained by the program can be presented in the form of:

$$\sigma = (302 + 1250\varepsilon^{0,3334}), \text{ MPa} \quad (3)$$

The thickness of the sheet metal from which the flat samples were cut was 4, 6, and 8 mm, however, a much larger number of samples subjected to testing were samples that were taken from a 4 mm thick sheet, because this thickness is dedicated to the mine destroyer's hull. The values of the determined Young's modules are close to the values characteristic for steel, which allows the tensile test to be considered correct.

Tab. 2 and fig. 2 show the mechanical properties read from true characteristics for flat samples taken from a steel sheet dedicated to the hull structure plating. They show that with a constant yield strength value in relation to the nominal values (about 550 MPa), the tensile strength limit changes. The average tensile strength limit is 1150 MPa ( $R_m$  approx. 850 MPa nominal) with strain reduced by 20% on average.

By comparing the mechanical properties of true characteristics for flat samples, it is difficult to show the influence of the rolling direction on the results, since there is no large dispersion in the values of yield strength and tensile strength, while for samples taken along the rolling direction, an increase in maximum elongation and strain is visible.

Comparison of the mechanical properties of the tested steel indicates that for samples taken perpendicular to the rolling direction, the strength limit is reduced by 4.7% with a reduced strain equal to  $\varepsilon = 2.01\%$ , the yield strength decreased by 1.78% with the corresponding strain reduced by  $\varepsilon = 16.5\%$  in relation to the mechanical properties of the samples taken perpendicular to the rolling direction occurs.

For flat 1.3964 steel samples, the difference between the tensile strength limit determined from true characteristics is 35.5% larger for samples taken along the rolling direction and 28.9% larger for samples taken perpendicular to the rolling direction.

## Welded joints

The next stage of the work was to examine the strength properties of welded joints. For this purpose, a set of samples was prepared, which was subjected to a static tensile test. Welding of 4 mm thick steel was carried out at Remontowa Shipbuilding SA in order to obtain identical welded joints as on the 258 project hull structure. Welding was performed by two methods of welding inert gas shielding (TIG) manually and semi-automatically. This approach should reduce the heat impact zone due to minimizing the heat exposure time for welding.

Then a static tensile test in order to obtain the actual material curves using DIC and the methodology described in [11] was carried out. Selected curves for the tests of welded joints made using the TIG method compared to the proposed Johnson – Cook material model (3) are presented (fig. 3).

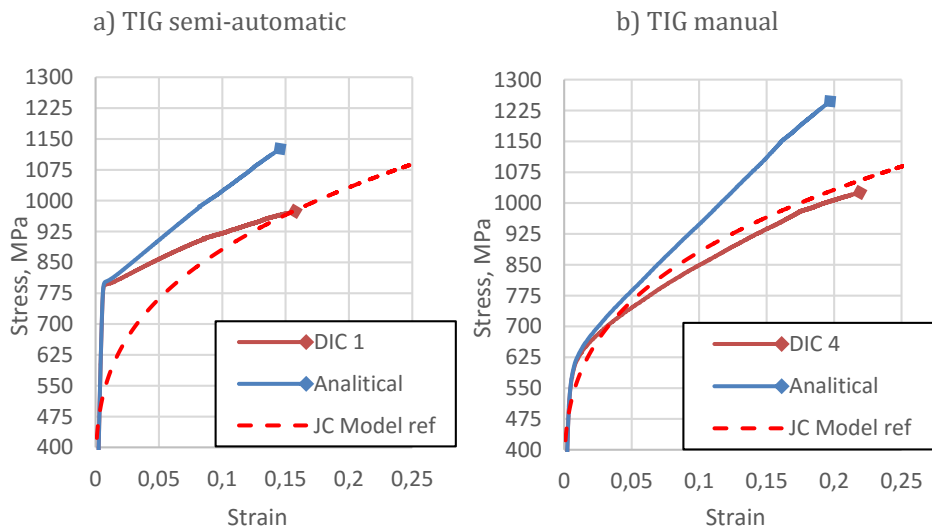


Fig. 3. Characteristics obtained by the DIC and analytical method of welded 1.3964 steel joints

Samples of welded joints were usually damaged in the base material (NM), outside the weld area (fig. 4). Cracking of welded joints took place outside the weld, the fusion line and the heat affected zone (HAZ). Samples cracked in the base material, which shows that the strength of the weld itself is greater than the welded steel.



Fig. 4. Examples of samples for which the crack occurred in base material

However, for one case a crack was noted not in the base material. Based on the hardness tests, the width of the heat affected zone was determined to be approximately 10 mm from the edge of the weld. The fracture occurred on the zone border (fig. 5). The course of the stretching curve for the discussed case differs from the other samples and the material model. Therefore, it was decided to compare the material characteristics of the reference (non-welded) sample with welded samples. The results are shown in fig. 6.



Fig. 5. Sample damaged at the edge of a heat affected zone

Knowing the true curves for welded joints, the JC model for welded joints was calculated using the procedure developed in MATLAB. Material constants for the weld model were proposed in the form:

$$\sigma = (729 + 689\varepsilon^{0,555}), \text{MPa} \quad (4)$$

The curve fitting developed by the program is shown in fig. 7, while a comparison of the base material model with the welded joint model is shown in fig. 8.

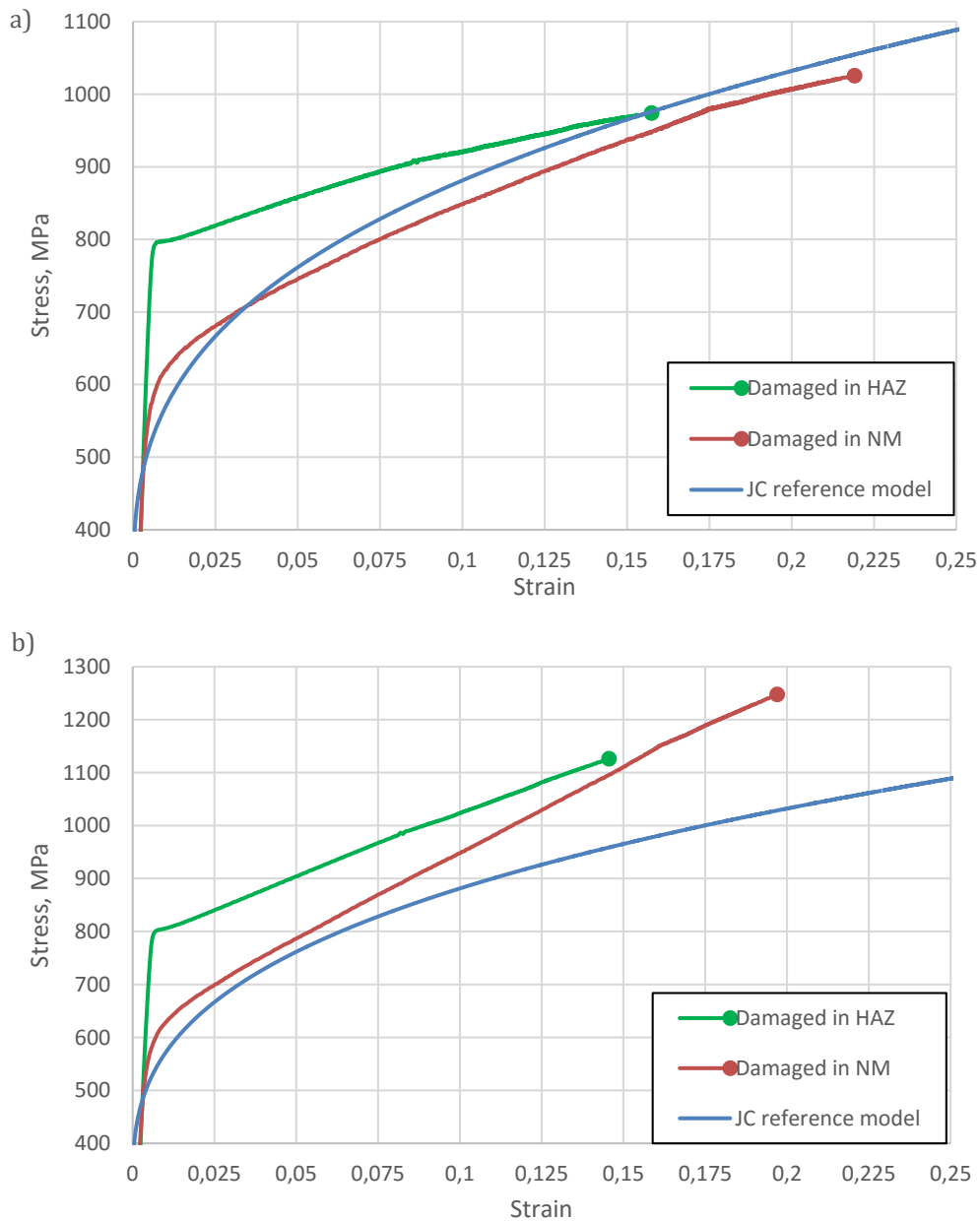


Fig. 6. Comparison of material characteristics determined by the DIC (a) and analytical (b) methods in relation to the JC model (3)

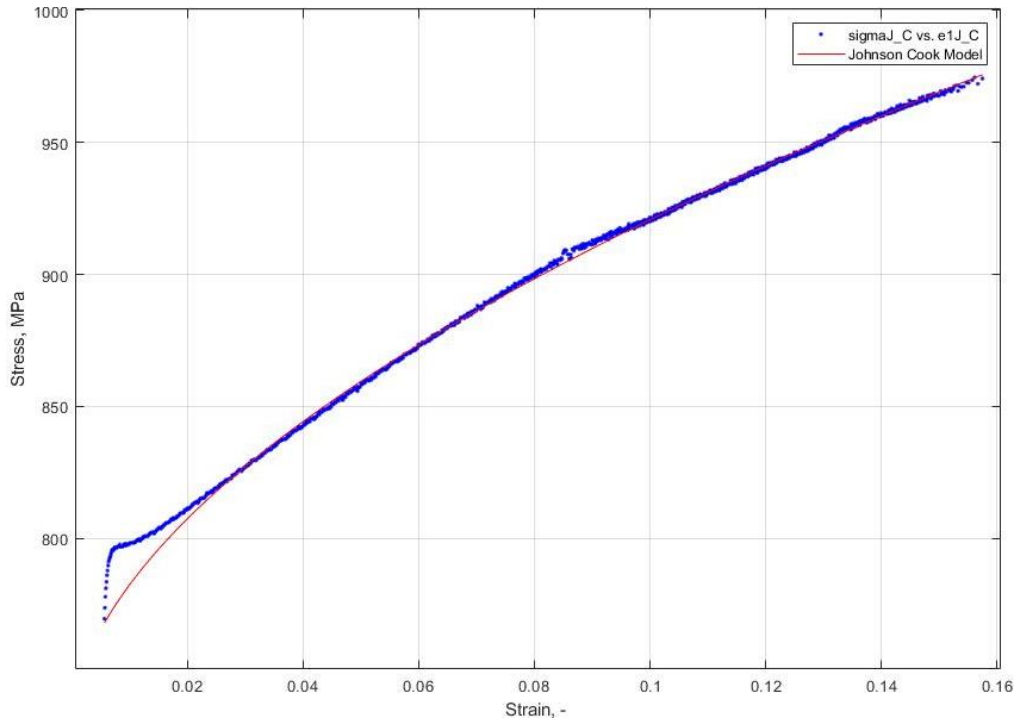


Fig. 7. Curve fitting for the material model developed in MATLAB

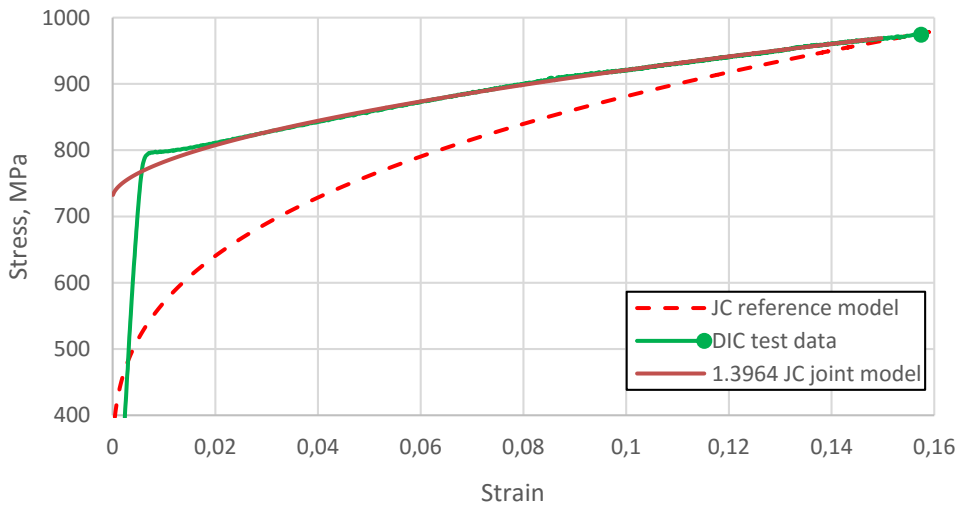


Fig. 8. Material curves developed for the needs of CAE welded joints strength analysis

## SUMMARY

The article presents tests of mechanical properties of 1.3964 steel and its welded joints. Johnson – Cook material model for welded joints was proposed. Despite the differences in the welded joint model from the base material, its usefulness may be necessary in specific cases for significant welded joints of a structure. Designers should be aware of the differences arising from the course of material curves during calculations using CAE.

Tests of mechanical properties of welded joints made using the digital image correlation method indicated a yield strength for welded joints at the level of 600 MPa for TIG manually and 800 MPa for TIG semi-automatically fig. 6.

The strength limit depends on the calculation methodology used. In the case of DIC it coincides with the values related to the reference sample, however, it refers to a different strain. In the case of analytical methodology, it is higher by a maximum of 200 MPa in relation to the theoretical strength limit, maintaining relatively high plastic deformations. The value of plastic deformation of welded joints meets the required Polish Register of Shipping.

The cracking area of the tested welded joints, which took place in the base material, showed that the strength of the welded joints (welds, penetration lines and heat affected zone) is greater than the strength of the base material. It follows that the material characteristics of the weld and base material should be of a similar nature. However, there are some differences resulting from the impact of welding temperature, because there was a decrease in the plasticity of welded steel by approx. 10–15%, which is common when increasing the hardness of the material.

In addition, one should consider the validity of the methods used to determine the actual material characteristics. The article shows the difference between the analytical and DIC method (fig. 6). The discrepancies should be verified by a more thorough analysis of the DIC method and factors affecting its unreliability. However, in engineering practice, the JC model is sufficient, which coincides well enough with the results of experiments in the field of plastic strain up to 10%.

## REFERENCES

- [1] Brózda J., *New-generation austenitic steels used for power equipment with supercritical parameters and their welding*, 'Bulletin of the Polish Welding Centre of Excellence', 2006, 5, pp. 40–48.

- [2] Johnson G. R., Cook W. H., *A constitutive model and data for metals subjected to large strains, high strain rates and high*, 'Proceedings of the Seventh International Symposium on Ballistics, 2009.
- [3] Jurczak W., Zatorski Z., Szturomski B. et al., *Wyznaczenie rzeczywistych dynamicznych charakterystyk wytrzymałościowych stali austenitycznej oraz stopów aluminium*, sprawozdanie z pracy badawczej statutowej pk. Austenka [*Determination of true and dynamic strength characteristics of austenitic steel and aluminum alloys*, report on statutory research under the Austenka code — available in Polish], Publ. Polish Naval Academy, Gdynia 2019.
- [4] *Kolejne etapy budowy okrętów typu 'KORMORAN II'* [*Next stages of construction of 'KORMORAN II' ships* — available in Polish], Remontowa Shipbuilding, [online], <http://www.remontowa-rsb.pl/aktualnosci/kolejne-etapy-budowy-okretow-typu-kormoran-ii/> [access 02.04.2020].
- [5] Kong L. Z., Shuai J., Zhou X. Y. et al., *True stress-logarithmic strain curves test of pipeline steels using 3D digital image correlation*, 'Optoelectronics and Advanced Materials — Rapid Communications', 2015, Vol. 9, No. 11–12, pp. 1380–1388.
- [6] *Lincoln Electric. Katalog materiałów spawalniczych Lincoln Electric* [*Lincoln Electric welding consumables catalog* — available in Polish].
- [7] *Metalcor 1.3964, Alloy 50*, Metalcor GmbH, Essen, Germany.
- [8] *Open the forge*, Voestalpine BÖHLER Edelstahl GmbH & Co KG catalog, 2019.
- [9] Polish Norm PN-EN ISO 6892-1:2009. *Metallic materials. Tensile testing, Part 1, Method of test at room temperature*, Polish Committee for Standardization, 2009.
- [10] Sosiński A., *Spawanie metodą TIG nie tylko dla początkujących* [*TIG welding not only for beginners* — available in Polish], Warszawa 2013.
- [11] Szturomski B., *Inżynierskie zastosowanie MES w problemach mechaniki ciała stałego na przykładzie programu ABAQUS* [*Engineering application of FEM in problems of solid mechanics on the example of the ABAQUS program* — available in Polish], Publ. Polish Naval Academy, Gdynia 2013.

## **WŁAŚCIWOŚCI MECHANICZNE POŁĄCZEŃ SPAWANYCH STALI 1.3964**

### **STRESZCZENIE**

W artykule przedstawiono wyniki badań właściwości mechanicznych połączeń spawanych stali, z której zostało wykonane poszycie kadłuba współczesnego niszczyciela min. Od wytrzymałości tych połączeń zależy utrzymanie szczelności przedziałów okrętowych w czasie eksploatacji. Zaprezentowano wyniki badań właściwości mechanicznych stali 1.3964 i jej połączeń spawanych poddanych statycznej próbie rozciągania oraz zaproponowano model materiałowy Johnson – Cook.

Model materiałowy może zostać wykorzystany w symulacji komputerowej CAE obciążenia kadłuba okrętu wykonanego z badanej stali.

Słowa kluczowe:

komputerowe wspomaganie projektowania (CAE), stal austenityczna, rzeczywiste charakterystyki materiałowe, spawanie.

---

*Article history*

Received: 02.04.2020

Reviewed: 16.04.2020

Revised: 18.04.2020

Accepted: 26.04.2020



## ACCESSIBILITY AND USABILITY OF LANDSAT 8 DATA FOR THE PURPOSE OF SATELLITE-DRIVEN BATHYMETRY OF THE SOUTH BALTIC NEAR-SHORE WATERS ON THE EXAMPLE OF GULF OF GDAŃSK

Karolina Zwolak\*<sup>1</sup>, Łukasz Marchel\*<sup>2</sup>, Marcin Skóra\*<sup>3</sup>,  
Radosław Przybysz\*<sup>4</sup>, Rafał Józwiak\*<sup>5</sup>, Kinga Tomaszewska\*\*

\* *Polish Naval Academy, Faculty of Navigation and Naval Weapons, Śmidowicza 69 Str., 81-127 Gdynia, Poland; e-mail: k.zwolak@amw.gdynia.pl, l.marchel@amw.gdynia.pl, m.skora@amw.gdynia.pl, r.przybysz@amw.gdynia.pl, r.jozwiak@amw.gdynia.pl; ORCID ID: <sup>1</sup>0000-0002-5540-4710, <sup>2</sup>0000-0003-1692-9175, <sup>3</sup>0000-0003-0309-2185, <sup>4</sup>0000-0002-1240-1261, <sup>5</sup>0000-0001-7513-6672*

\*\* *3rd Ship Flotilla, Rondo Bitwy pod Oliwą 1 Str., 81-103 Gdynia, Poland; e-mail: k\_tom07@gmail.com; ORCID ID: 0000-0002-9564-1155*

### ABSTRACT

The paper presents the analysis of accessibility and usability of Landsat 8 Satellite Imagery for the purpose of Satellite Derived Bathymetry (SDB) products generation of the area of near-shore waters of the Polish coast. General assumptions of the SDB, Landsat program and factors affecting the products generation process have been described in details. Examples of SDB results, generated using both GIS software and Matlab, are presented on the example of chosen areas of Gulf of Gdańsk. The advantages and disadvantages of the SDB method are presented in the discussion and conclusion part with the proposed directions for the future works.

#### Keywords:

Satellite Derived Bathymetry, Landsat 8, bathymetric survey.

#### Research article

© 2020 K. Zwolak, Ł. Marchel, M. Skóra, R. Przybysz, R. Józwiak, K. Tomaszewska  
This is an open access article licensed under the Creative Commons  
Attribution-NonCommercial-NoDerivatives 4.0 license  
(<http://creativecommons.org/licenses/by-nc-nd/4.0/>)

## INTRODUCTION

As soon as people began to exploit maritime areas, initially for transport purposes, it was immediately necessary to obtain a reliable information about what is under the water surface to ensure the safety of navigation. Shoals, rocks or wrecks of the first sunken ships have always posed a threat to vessels. Then ideas began to appear on how to get this information. Over the years of experience, these methods have been improved, and today it is possible to choose from many available, depending on the user's needs and capacity. Single and multibeam echosounders or interferometric side scan sonars provide mariners with the accurate data about seafloor depths at literally all the possible depth ranges, although its manufacturing and operation is labor-intensive and extremely expensive. Further shallow water can be covered by LiDAR devices, but airborne equipment on traditional aircraft is expensive to use and not widely available.

At the same time the satellite technology has been developed for various purposes, including positioning and surveillance applications. Later, the possibility of obtaining information about depths of any waterbody without the need of direct measurements in these places seems to be a promising vision of the future hydrography. To do this, only access to photos taken by satellites and the ability to process the image into a bathymetric map product would be required. The current level of advancement and continuous development of a technology is able to partially provide these needs. However, there are still some limitations that neither man nor any device can overcome. Therefore, we are talking mainly about atmospheric conditions and the properties of the sea water, which may have a negative impact on the possibility of using satellite images to create accurate bathymetric maps.

## LANDSAT 8 IMAGERY DATA

Landsat satellite system was created in early 70s of the last century, as a part of a cooperation between the two American leading research centers — NASA (National Aeronautics and Space Administration) and USGS (United States Geological Survey). Over the decades, the system has been modernized by introducing the satellites numbered according to the chronology of the process of their location on the near-polar orbit. The operational part of the system is now composed of one satellite, designed for remote data acquisition, and the Earth-based control station. Images

are collected in several sub-ranges of the electromagnetic spectrum. The full spectrum used by Landsat 8 is divided into 11 sub-bands [3]. Tab. 1 shows the sub-ranges used by the Landsat 8 Operational Land Imager (OLI) and Thermal Infrared Sensor (TIRS).

Tab. 1. Landsat-8 sensor OLI & TIRS bands [3]

Landsat-8 sensor OLI & TIRS bands ( $\mu\text{m}$ )			
Sub-range	Description	Wavelength( $\mu\text{m}$ )	Resolution (m)
Band 1	<i>Coastal / Aerosol</i>	0.435 to 0.451	30
Band 2	<i>Visible blue</i>	0.452 to 0.512	30
Band 3	<i>Visible green</i>	0.533 to 0.590	30
Band 4	<i>Visible red</i>	0.636 to 0.673	30
Band 5	<i>Near-infrared</i>	0.851 to 0.879	30
Band 6	<i>Short wavelength infrared</i>	1.566 to 1.651	30
Band 7	<i>Short wavelength infrared</i>	2.107 to 2.294	60
Band 8	<i>Panchromatic</i>	0.503 to 0.676	15
Band 9	<i>Cirrus</i>	1.363 to 1.384	30
Band 10	<i>Long wavelength infrared</i>	10.60 to 11.19	100
Band 11	<i>Long wavelength infrared</i>	11.50 to 12.51	100

Information is processed according to the selected sub-bands for the needs of a cartography, an agriculture, an assessment of changes on the Earth, geology and many others. Images are available for free and can be downloaded from the official USGS website (<https://earthexplorer.usgs.gov>). User interface is presented on fig. 1.



Fig. 1. User interface [<https://earthexplorer.usgs.gov/>]

The satellite works at an altitude of 705 km and is powered by solar panels. The batteries power the satellite when there is no solar energy input. The main orbital parameters are: the average period is 99 minutes and the inclination is equal to 98.2 degrees. The satellite is equipped with two types of sensors: Operational Land Imager (OLI) and Thermal Infrared Sensor (TIRS). Sensors can work independently of each other. OLI is the main imaging instrument installed on Landsat 8. This sensor records the imagery in 9 sub-ranges of visible and invisible bands. The resolution is 30 m or 15 meters, depending on the band. The OLI type sensor has been designed to function for 5 years from the date of commissioning. Thermal Infrared Sensor is the second sensor installed on the satellite. TIRS gathers images of the Earth in sub-range spectrum emitted by the Earth's Surface according to the temperatures of particular areas. Landsat 8 uses two types of radio frequency antennas: the S-band is used to control the satellite and X-band used to send imagery to the control station [3].

There are a number of products derived from the collected imagery and released by the USGS for end-users. Data used in this paper are downloaded from 'Landsat 8 OLI/TIRS C1 Level-1' subset of 'Landsat Collection 1 Level 1'.

### **CHARACTERISTICS OF POLISH COASTAL WATERS IN TERMS OF SATELLITE IMAGERY ACQUISITION**

Satellite imagery acquisition of coastal water areas for the purpose of bathymetry assessment is mostly affected by two factors: weather conditions and water clarity.

According to [6] Baltic Sea watermasses are characterized by high levels of suspended matter and Colored dissolved organic matter (CDOM), with the origin of nearby land areas. The suspended material strongly influences the Sun light penetration. Brownish color characterizes the large amount of CDOM in the Baltic waters. The inversion from optical measurements into water properties, due to the fact of multi-componential water characteristic, cannot necessarily be unique. It can highly affect the accuracy of image analysis based methods results [6]. Similar analysis are presented in [15].

Cloudiness is the weather condition, which in many cases disqualifies the acquired image from further analysis. For the Polish coast the cloudiness is significant throughout the year. From March to September, averagely 6/10 of the sky is covered

with clouds. May and June are the sunniest months. In the rest of year months the average cloud cover ratio is 7/10 and in December 8/10. The average annual number of cloudy days is 112–160 and sunny days is 22–47. Cloudy days in the coastal zone usually occur from October to March and sunny days from April to September [1, 4].

Fig. 2 presents the percentage of cloud cover and the sun elevation for all the Landsat 8 images collected over the Gulf of Gdańsk, from 2014 to 2019. The data from all the images with the cloud coverage less than 10% have been summarized in tab. 2 Note, that only 16 images from 121, can be used for the wider analysis of Earth surface, the rest is partially or fully covered by clouds.

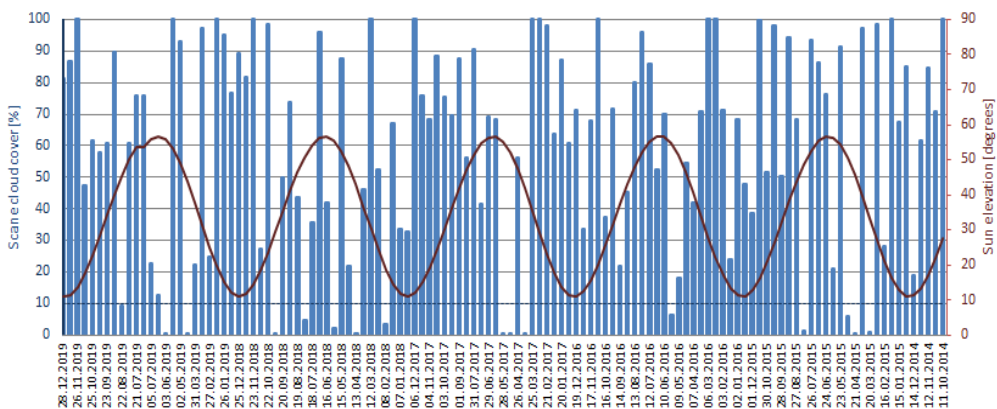


Fig. 2. The percentage of cloud cover (blue) and the sun elevation (dark red), for Landsat 8 images collected over the Gulf of Gdańsk, from 2014 to 2019

Tab. 2. The summary of all the images with the cloud coverage less than 10% collected over the Gulf of Gdańsk, from 2014 to 2019

<b>Date</b>	<b>20.03.2015</b>	<b>21.04.2015</b>	<b>07.05.2015</b>	<b>11.08.2015</b>	<b>25.05.2016</b>	<b>10.04.2017</b>	<b>12.05.2017</b>	<b>28.05.2017</b>
<b>Cloud cover [%]</b>	0.95	0.09	5.99	1.64	6.28	0.04	0.06	0.02
<b>Sun elev. [deg]</b>	33.45	45.64	50.59	48.71	54.77	41.89	52.05	55.19
<b>Date</b>	<b>08.02.2018</b>	<b>13.04.2018</b>	<b>31.05.2018</b>	<b>03.08.2018</b>	<b>06.10.2018</b>	<b>16.04.2019</b>	<b>03.06.2019</b>	<b>22.08.2019</b>
<b>Cloud cover [%]</b>	3.50	0.08	2.27	4.63	0.03	0.04	0.03	9.24
<b>Sun elev. [deg]</b>	18.71	42.90	55.50	50.71	29.44	43.9	55.9	45.8

The ice cover can also affect the usefulness of satellite acquired images, although shipping conditions in the South Baltic are favorable. In open areas in 75–90% of all winters ice phenomena do not occur. Along Polish coasts, ice is not present in 50–75% of all winters [1, 4].

## **BATHYMETRY ASSESSMENT BASED ON THE SATELLITE IMAGERY**

There is a number of works mentioning the Satellite Derived Bathymetry, as one of the ways to obtain information about the depths of waters. They are presented in this section. The authors of these works already in the introductions of their publications clearly indicate the possibility of using satellite bathymetry only in the shallow waters of coastal areas, which is characteristic for all the bathymetric measurement techniques based on the Sun light penetration, due to the fast attenuation in the water column.

Theoretical fundamentals for Satellite Derived Bathymetry have been built by David Lyzenga, in 1978 [7]. Three years later he published the developments of his methods [9]. In his considerations he took into account both photos taken from one of the Landsat satellites and obtained using a multispectral scanner located on an aircraft. After proper treatment and comparison with the existing maps of the examined area, he found an advantage in the accuracy of images from the scanner over satellite. As the reason he gave, among others, the fact that the quality of satellite images depends on weather conditions, especially cloud cover. Sometimes a cloud cover completely prevents further use of images, as well as errors in the operation of the algorithm creating the final bathymetric product. However, the SDB, assessed as a trade-off between the map accuracy and the method availability, proved its validity as a reconnaissance tool. His thesis have been also developed in his and his co-authors later publication [8].

The author who also noticed the dependence of bathymetric map accuracy on meteorological conditions is William Philpot [13]. However, he paid more attention to the hydrology of the study area than the impact of the atmosphere. In his work, he developed research results indicating that satellite bathymetry will only fulfill its role in places where the conditions in the water are characterized by low variability. We are talking here mainly about the mixing of water layers, the occurrence of flowering vegetation in different seasons and the movement of bottom sediments. All these factors affect the occurrence of errors during photo processing due to the different reflecting properties of different types of seabed or plant density. Then, the reflected wave returning to the satellite will not correctly indicate the depth in the investigated water.

The most fundamental paper for the Satellite Derived Bathymetry is [14]. The paper describes the modern methodology, applied nowadays for depth determination applications using satellite imagery of different types.

A lot of works in the field of Sattelite Bathymetry have been done by the team lead by Shachak Pe'eri. They assessed SDB methods in various conditions and published their results in [10–12].

Note, that in many cases in this paper the term 'bathymetric product' is used instead of 'bathymetric map' or 'chart'. Although the difference between map and chart is obvious in the nautical literature, the 'product' may seem to be not understood. The reason to avoid the word 'map' is not to infer that the SDB truly depicts the real shape of the seafloor. There are such a number of restrictions, under SDB algorithms are utilized, so the effect should be understood as an algorithm result only — means a product — not a map.

Bathymetric product generation procedure starts with extraction of the subset of usable images from the complex dataset downloaded from the Landsat imagery depository. Images must be selected based on time, we are interested in, but also based on the environmental conditions, which includes the cloud coverage and sun glint. Recommended SDB bands from Landsat 8 are presented in tab. 3.

Tab. 3. Landsat 8 bands recommended for the SBD procedure [5]

Platform	Band	Image number in dataset	Wavelength (µm)
Landsat 8	Blue	2	0.45–0.51
	Green	3	0.53–0.59
	Infrared	6	1.57–1.65

Downloaded imagery format (GEOTIFF) suggests using the Geographic Information System software. ArcMap 10.5.1 has been used for the image processing. Authors of [5] presents the tutorial of bathymetric products generation using ArcGIS. Setting up the workspace in ArcMap, importing the appropriate charts for reference and importing downloaded imagery (fig. 3a) are the parts of preprocessing before the whole procedure.

Infrared (IR) image is used for land/water separation. Profile Graph tool in ArcMap can be used for determining the value of threshold, separating the wet and dry areas, clearly visible on the infrared imagery. In case of Landsat 8 images, the threshold value is usually around 5500. The values corresponding to the pixels representing the water body are below 5000, while the highest values on land reach around 16000. The boundary between land and water is delimited by a very clear, rapid values difference. Generated matrix indicating water bodies is then used for water body extraction on remaining images (fig. 3b).

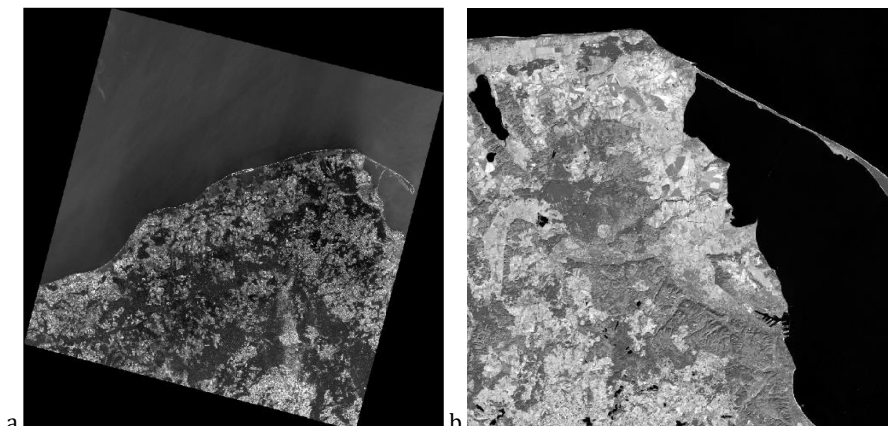


Fig. 3. (a) Blue and green bands uploaded into the ArcMap software (the last one on top);  
(b) Infrared band matrix used for water bodies extraction

Next step is derived from the ratio approach, presented in [14], which says that the actual depth at a given point is proportional to the ratio of natural logarithms of reflectance values of blue and green band at the corresponding pixel of the multispectral imagery (Equation 1):

$$Z = m_1 \frac{\ln(nR_w(\lambda_i))}{\ln(nR_w(\lambda_j))} - m_0, \quad (1)$$

where:

- $m_1$  — tunable constant to scale the ratio to depth;
- $m_0$  — the offset for a depth of 0 m;
- $R_w(\lambda_i)$  — reflectance values of blue band;
- $R_w(\lambda_j)$  — reflectance values of green band;
- $n$  — a fixed constant for all areas, chosen to assure both that the linear response with depth will be produced and the logarithm will be positive under any condition.

The values of logarithms ratios ( $\ln(nR_w(\lambda_i))/\ln(nR_w(\lambda_j))$ ) creates the surface called the Bathymetry Algorithm Surface (here: the BA Surface — fig. 4). It's values are linearly proportional to the depths down to the specific depth, called the Extinction Depth; beyond that there is no linearity in the values-depths dependence. The Extinction Depth is characteristic for a particular area, depends on the optical properties of the water and determines the usability of Satellite Derived Bathymetry method for the analyzed region.



Fig. 4. Bathymetry Algorithm Surface in ArcMap

While the logarithms ratio values for each pixel are conducted from the imagery only, determining the  $m_1$  and  $m_0$  values requires the use of control points. Andrzej Chybicki in [2] uses the results of bathymetry measurements conducted on the profiles perpendicular to the coast line and the prevailing direction of isobaths, which provides the reference at various depths. This is very appropriate approach, although requires dedicated survey, conducted on the vessel capable of operating at very shallow depths. Another possibility is to use the survey conducted for general safety of navigation purposes and published in the form of ENC or nautical chart soundings or to use point cloud or grid data from those surveys, depending on the resources available for a specific area (fig. 5a).

Bathymetric products are created region-wise; it means that the values from the specified basin are analyzed at once, by masking it by the polygon designed to include the depths from a specified range, from the shallowest possible to exceeding the expected Extinction Depth. The examples are presented in fig. 5b.

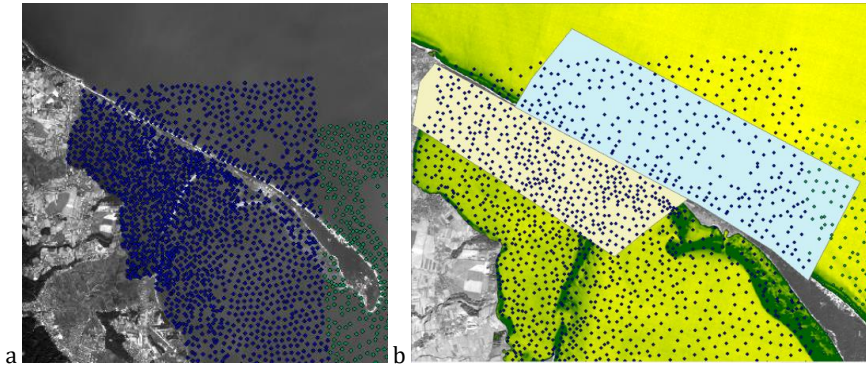


Fig. 5. (a) The locations of ENC soundings derived from the ENC cells produced by the Hydrographic Office of the Polish Navy; (b) Example polygons generated to extract depth data and compare with BA Surface

After plotting the reference depths against the corresponding values from the BA surface, we are able to estimate the Extinction depth, by determining the depth value on the plot, above which we are not able to observe the approximately linear dependency between plotted values (fig. 6a). The subset of data, below the Extinction Depth is used for SDB depth determination, by generating a trend line (fig. 6b). The Extinction Depth value assumed here for further analysis was 5 m.

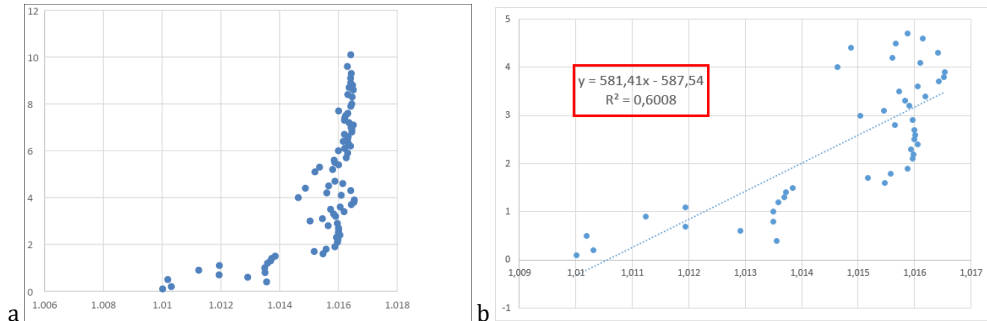


Fig. 6. (a) The reference depths plotted as a function of the corresponding values from the BA surface; (b) The trend line with its coefficients, generated for the subset of data with linear dependency

By applying the gain and the offset coefficients according to Equation 1 to the BA surface, we are getting the Satellite Derived Bathymetry Product (SDB Bathymetry) and this is called the referencing operation. After limiting the results to the range within the Extinction Depth value, we can present the results in the form of a map (fig. 7).

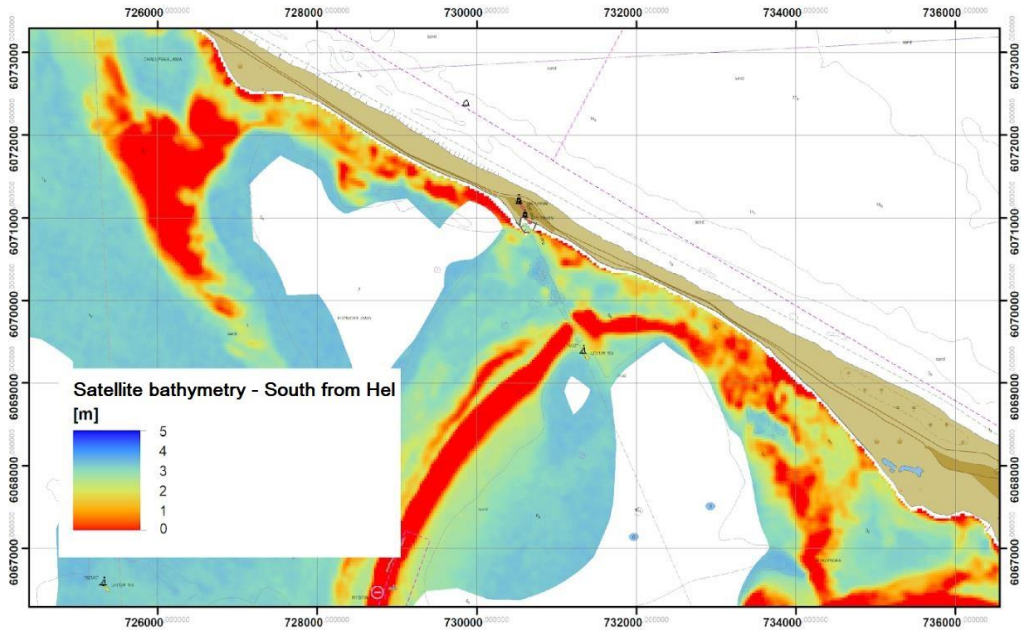


Fig. 7. The result of Satellite Bathymetry Algorithm — an example area, South to the Jastarnia harbour on the Gulf of Gdańsk

The full Satellite Bathymetry algorithm implementation is in fact a series of steps, which can be done in GIS software, but they can also be coded to automate all the stages of product generation. The application to automatically generate the surfaces has been written in Matlab and utilized for fast product generation of the series of images collected over the same area from 2015 to 2019. This allows us to observe the changes of the analyzed area over the chosen period of time. It was noticed that to observe only the fact of the changes, caused by sediment movements, it is enough to generate the BA Surfaces and compare them. The example is presented in fig. 8. BA Surfaces have been presented in a grayscale. Dark areas indicate shallower depths. Isobaths on ENC are generated based on data from 2009. We can clearly see the conformity between color-indicated shallower areas with the isobaths from ENC on the images from 2015 to 2017. Later on, the sediments movement have been changing the general shape of the shoal, which can be observed on the generated imagery.

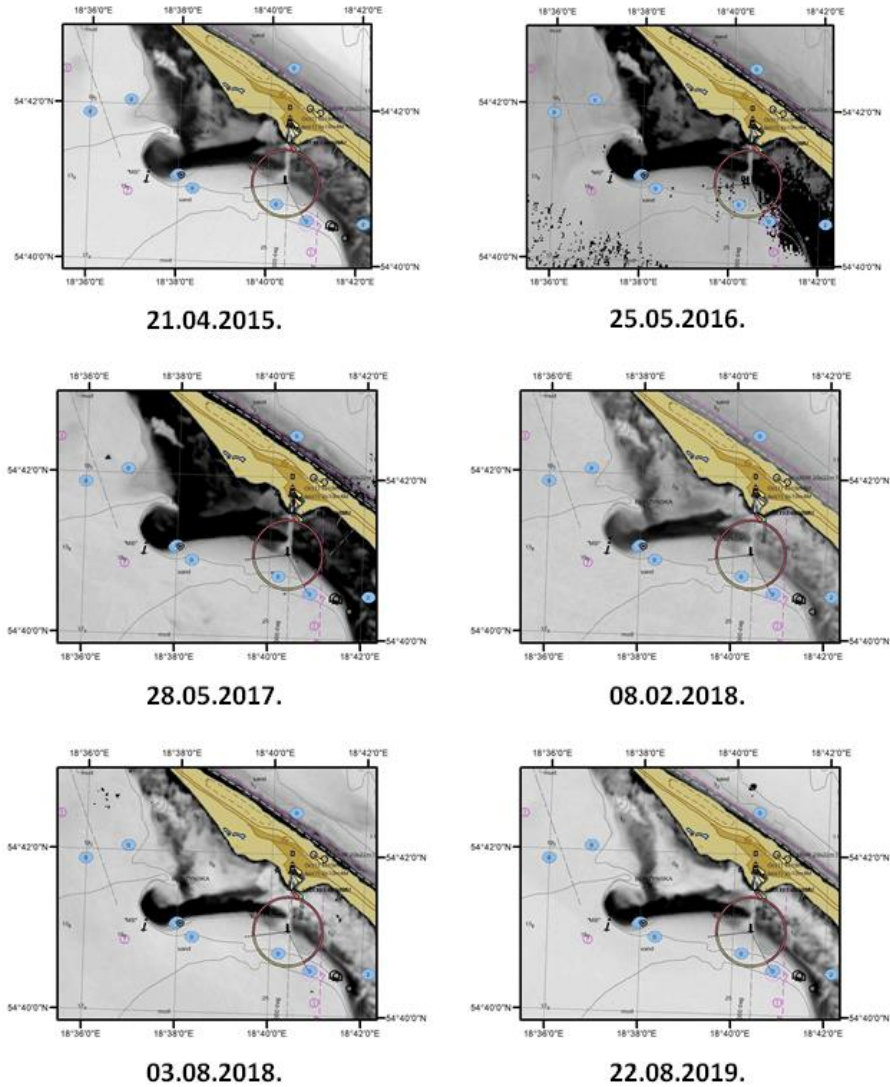


Fig. 8. BA Surfaces generated based on the Landsat imagery from 2015 to 2019

## DISCUSSION OF THE METHOD AND ITS POTENTIAL USE

Bathymetric maps were compared with the data from electronic navigation charts. Using this method, it is possible to immediately compare the depths obtained using SDB with those obtained with data acquisition methods of hydrographical

quality, for example using a multibeam echosounder. Such data is definitely more accurate and more reliable than satellite imagery derived bathymetry, so a comparison of the values on the maps will be carried out in relation to them, followed by an assessment of the suitability of bathymetric products from the satellite.

Often it can be seen that the bottom profile is arranged very similarly to the one determined using isobaths. Where there is a shallower area, there is indeed a color that indicates smaller depths.

Very often it can be noticed that satellite bathymetry tends to highlight values. In shallower places, according to the satellite map, the depth value is close to 0, while in deeper places these values are excessively large. At the same time, the bottom shape variability trend is maintained. This fact indicates the possibility of using satellite maps for purposes that do not require specific values, but only estimates or the detection of changes in time.

Looking at the satellite bathymetric maps, we can immediately see that they indicate depths only up to a certain value previously referred to as the Extinction Depth. Satellite Bathymetry does not allow to determine the deeper depths and this is the main restriction of this method.

Although there are few, there are some applications for which satellite bathymetric maps may be useful. Despite the occurrence of differences between SDB results and correct depth indications, these maps retain the ability to present general bottom formation. This feature is quite important from the perspective of the need to control the changes in the bottom of the studied water body and prioritize the areas for reliable hydrographic survey in places where any fault in the proper bathymetry data delivery may result in a vessel grounding. If the bathymetric satellite map notices changes in the location or shape of the shoal, it can be assumed that the area requires examination by another, more accurate method, which would result in a possible update of the navigation maps.

Along with the previously presented possibilities of using bathymetric satellite maps, there are also restrictions, which, as it turns out, are much more numerous. They mainly result from the inaccuracy of the data received and the limitation of the area shown on the map to the Extinction Depth. This limit particularly affects the scope of application of satellite bathymetric maps. Depending on the body of water, the depth of disappearance in the Baltic Sea ranges from about 5 to 8 meters. This means that below such depth, satellite bathymetry does not distinguish between values, so it presents the bottom as a uniform area. The restriction is therefore the possibility of using these maps only in coastal waters, whose depths are smaller than the determined Extinction Depth.

Weather conditions are another limitation affecting SDB. Pictures are taken by a satellite from a relatively high altitude, so any cloudiness over the photographed area affects the quality of the image received, and even causes its uselessness. The ratio of images affected by this phenomena for the Gulf of Gdańsk, achieved the level of 87%. When trying to generate the bathymetric map, it may turn out that all available satellite images were taken in cloud conditions. Then it will be impossible to obtain the bathymetric map using SDB. In this case, photos taken from the deck of the aircraft may be much more useful, which, in the event of adverse conditions, may be under the lower layer of clouds.

Staying with the subject of environmental conditions, one should pay attention to the relationship between satellite bathymetry and the characteristics of water in a given body of water. In the case of Baltic, its low transparency is a major limitation, which is also caused by increasing pollution. Less possibility of light penetrating the water layers may result in the wave not reaching the bottom, which in turn causes incorrect determination of the depth at this point. The dark color of the water is also affected by the periodic occurrence of various types of vegetation, which can give the confusing impression of shallow areas.

The usability of Satellite Derived Bathymetry products is also affected by the low resolution of available imagery. The resolution of Landsat 8 imagery is 30 m, which allows using only to general analysis of a given area, without resolving any minor features.

## **CONCLUSIONS AND THE DIRECTIONS OF FURTHER RESEARCH**

The SBD method has a significant advantages. The large footprint of 185 km provide a lot of useful data. The method is repeatable, easily accessible and can be used as an alarm to pay attention for a specific areas There are some drawbacks in the method described and used in the paper, that make it limited and dependent on many factors. Many of them are independent of the user and cause that obtaining accurate bathymetric data for a given moment may not be possible. Therefore restrictions associated with cloud coverage of the analyzed area could be eliminated by using images of sea areas taken by Unmanned Aerial Vehicles (UAV). Their operational altitude is between 10 and 150 meters. This altitude is significantly below the cloud layer. Taking such measurements also results in a significant increase of the accuracy and resolution of the acquired imagery. Mostly aerial photos from unmanned

aerial vehicles have a resolution of a few centimeters per pixel. Such accuracy translates into a much higher number of measurements per study area and increases the potential range of use.

However, the UAV method also has some limitations that must be indicated. First of all, the limited range and short battery life of the UAV battery will certainly cause that the waters far away from the operator (shore, beach) cannot be covered with aerial photographs. Another issue that needs to be highlighted is the limited possibility of georeferencing of aerial photographs taken over sea areas (reservoirs). To obtain high accuracy of position coordinates projected on a photograph (matrix of pixels), it would be necessary to carry out a georeference procedure using a high accuracy GNSS receiver (using RTK corrections) and a fixed infrastructure. These elements must be easily distinguishable in aerial photographs and assigned to the coordinates of their positions. Examples of two possible cases are presented in fig. 9.

The use of single aerial photographs may be a big limitation to the proposed method due to the low coverage of the sea area in the photograph and the need for georeferencing. The use of an orthophoto map of a coastal area made up of many interrelated aerial photos can solve the problems mentioned above. However, one should be aware that in the sea area the accuracy of position coordinates of particular points on the study will be degraded. Another restriction is associated with the process of building an aerial orthophoto map. This method is based on a combination of overlapping photos based on a search of their common elements (found on both or more photos). The common area (overlap) is interpolated on the basis of many photographs in which it is distinguishable. The indicated estimation may interfere with the real colors of individual points of the environment, because the photographs used in the process are not taken at the same time. An example is presented in fig. 10.

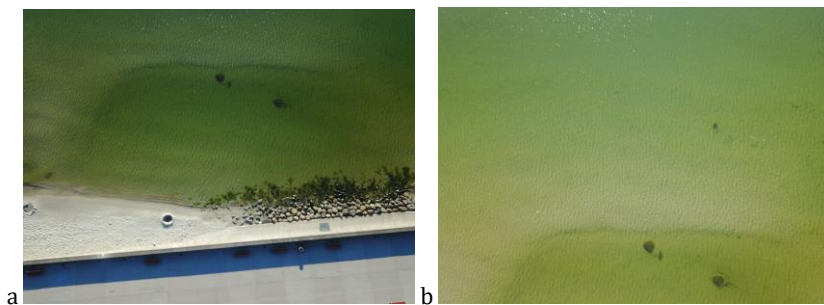


Fig. 9. (a) Part of the Gulf of Gdańsk, which can be georeferenced; (b) Part of the Gulf of Gdańsk which cannot be georeferenced due to no distinguishable objects or infrastructure



Fig. 10. Władysławowo harbour orthophoto map — many imperfections situated on the water surface

The UAV method's characteristic induce them to be used only in internal waters and coastal waters, where the land infrastructure exists at short distances (which can be used in the georeferencing process). However, from the point of view of the content presented in the paper, it seems justified to verify the assumptions presented here in the further work.

Overall, the SDB technique has many advantages as a reconnaissance tool for charts update, chart adequacy control and for risk assessment. The integration of different methods, for example the SDB method with the UAV, can lead to the accurate result, sufficient for continues shallow areas monitoring.

#### **Acknowledgments**

This work has been funded by the Polish Naval Academy statutory funds for young researchers.

## REFERENCES

- [1] Biuro Hydrograficzne Marynarki Wojennej, *Locja Bałtyku 502*, Gdynia 2008 [*Sailing Directions. Baltic Pilot* — available in Polish].
- [2] Chybicki A., *Mapping South Baltic Near-shore bathymetry using Sentinel-2 observations*, 'Polish Maritime Research', 2017, Vol. 24, No. 3 (95), pp. 15–25, DOI: 10.1515/pomr-2017-0086.
- [3] Department of the Interior U.S. Geological Survey, *Landsat 8 (L8) Data Users Handbook*, Version 5.0, November 2019.
- [4] Håkanson L. (ed.), *Charakterystyka fizycznogeograficzna zlewiska Morza Bałtyckiego* [*The physical and geographical characteristics of Baltic Sea watershed*], trans. A. Jankowski, G. Jankowski, 'Środowisko Morza Bałtyckiego', 1991, 1.
- [5] International Hydrographic Organization, Intergovernmental Oceanographic Commission, *The IHO-IOC GEBCO Cook Book*, IHO Publication B-11, Monaco, Sep. 2018, 416 pp – IOC Manuals and Guides 63, France, September 2018.
- [6] Leppäranta M., Myrberg K., *Physical Oceanography of the Baltic Sea*, 2009, Springer.
- [7] Lyzenga D., *Passive Remote-Sensing Techniques for Mapping Water Depth and Bottom Features*, 'Applied Optics', 1978, Vol. 17, Issue 3, pp. 379-383, DOI: 10.1364/AO.17.000379.
- [8] Lyzenga D., Malinas N., Tanis F. J., *Multispectral bathymetry using a simple physically based algorithm*, 'IEEE Transactions on Geoscience and Remote Sensing', 2006, Vol. 44, Issue 8, pp. 2251–2259, DOI: 10.1109/TGRS.2006.872909.
- [9] Lyzenga D., *Remote sensing of bottom reflectance and water attenuation parameters in shallow water using aircraft and LANDSAT data*, 'International Journal of Remote Sensing', 1981, Vol. 2, pp. 71–82, DOI: 10.1080/01431168108948342.
- [10] Pe'eri S., Freire R., Klemm A., Nyberg J., *Satellite-Derived Bathymetry: Performance and Production*, 2016, Canadian Hydrographic Conference, May 16–19, 2016 Halifax, NS.
- [11] Pe'eri S., Madore B., Nyberg J., Snyder L., Parrish C., Smith S., *Identifying Bathymetric Differences over Alaska's North Slope using a Satellite-derived Bathymetry Multi-temporal Approach*, 'Journal of Coastal Research', 2016, No. 76 (sp 1), pp. 56–63, DOI: 10.2112/SI76-006.
- [12] Pe'eri S., Parrish C., Azuike C., Alexander L., Armstrong A., *Satellite Remote Sensing as Reconnaissance Tool for Assessing Nautical Chart Adequacy and Completeness*, 'Marine Geodesy', 2014, Vol. 37, Issue 3, pp. 293-314, DOI: 10.1080/01490419.2014.902880.
- [13] Philpot W., *Bathymetric mapping with passive multispectral imagery*, 'Applied Optics', 1989, Vol. 28, Issue 8, pp. 1569-1578, DOI: 10.1364/AO.28.001569.
- [14] Stumpf R., Holderied K., Sinclair M., *Determination of water depth with high resolution satellite imagery over variable bottom types*, 'Limnology and Oceanography', 2003, Vol. 48, pp. 547–556, DOI: 10.4319/lo.2003.48.1\_part\_2.0547.
- [15] Sylvain J., Guillaume M., Minghelli-Roman A., Deville Y., Chami M., Lafrance B., Serfaty V., *Hyperspectral remote sensing of shallow waters: Considering environmental noise and bottom intra-class variability for modeling and inversion of water reflectance*, 'Remote Sensing of Environment', 2017, Vol. 200, pp. 352–367, DOI: 10.1016/j.rse.2017.08.020.

# **DOSTĘPNOŚĆ DANYCH OBRAZOWYCH LANDSAT 8 I MOŻLIWOŚĆ ICH WYKORZYSTANIA W ALGORYTMACH BATYMETRII SATELITARNEJ DLA WÓD PRZYBRZEŻNYCH POŁUDNIOWEGO BAŁTYKU NA PRZYKŁADZIE ZATOKI GDAŃSKIEJ**

## **STRESZCZENIE**

W artykule przedstawiono analizę dostępności i użyteczności zdjęć satelitarnych Landsat 8 na potrzeby generacji produktów batymetrii satelitarnej obszaru wód przybrzeżnych polskiego wybrzeża. Ogólne założenia SDB, programu Landsat i czynniki wpływające na proces wytwarzania produktów zostały szczegółowo opisane. Przykłady wyników SDB, wygenerowanych przy użyciu zarówno oprogramowania GIS, jak i Matlaba, przedstawiono na przykładzie wybranych akwenów Zatoki Gdańskiej. Zalety i wady metody oraz proponowane kierunki przyszłych prac przedstawiono w części podsumowującej.

### Słowa kluczowe:

batymetria satelitarna, Landsat 8, sondaż batymetryczny.

---

### *Article history*

Received: 04.03.2020

Reviewed: 15.04.2020

Revised: 19.04.2020

Accepted: 28.04.2020



## THE USE OF A MICROCONTROLLERS IN HYGROMETRIC MEASUREMENTS APPLICATION

Artur Bogdanowicz\*<sup>1</sup>, Marcin Zacharewicz\*<sup>2</sup>, Jakub Król\*\*

\* Polish Naval Academy, Faculty of Mechanical and Electrical Engineering, Śmidowicza 69 Str., 81-127 Gdynia, Poland; e-mail: a.bogdanowicz@amw.gdynia.pl, m.zacharewicz@amw.gdynia.pl; ORCID ID: 10000-0002-5076-6675, 20000-0002-8294-873X

\*\* Graduate Polish Naval Academy, Faculty of Mechanical and Electrical Engineering, Śmidowicza 69 Str., 81-127 Gdynia, Poland

### ABSTRACT

The article presents the possibility of using microcontroller systems as one of elements of a teaching position. The Arduino Mega system based on the ATmega 2560 microcontroller from the AVR family was used to build the station. At the beginning, a virtual hygrometer model was designed in the AUTOCAD program and then the air channels were made using 3D printing. After assembling the station, it was compared to a laboratory aspiration hygrometer. The analysis was presented in the final part of the article.

#### Keywords:

microcontroller system, hygrometer, laboratory station.

#### Research article

© 2020 Artur Bogdanowicz, Marcin Zacharewicz, Jakub Król  
This is an open access article licensed under the Creative Commons  
Attribution-NonCommercial-NoDerivatives 4.0 license  
(<http://creativecommons.org/licenses/by-nc-nd/4.0/>)

## INTRODUCTION

Already at the turn of the fifteenth and sixteenth centuries, attempts were made to study the change of water vapor content in the air. The first primitive hygrometers were based on the method of hygroscopic measurement, e.g. change in the weight of a woolen sphere absorbing moisture from the atmosphere. These studies contributed to the further development of this field, and other solutions and materials that absorb moisture have been sought [2, 4].

### MEASUREMENT OF AIR HUMIDITY USING A HYGROMETER

The psychrometer is a device from the family of hygrometers. The simplest consists of two thermometers, one of which is surrounded by a fabric soaked with distilled water, and shows temperature of the wet thermometer. And the other is an ordinary thermometer indicating the ambient temperature [1].

The measurement in the psychrometric method depends on the state of saturation with the steam of the air flowing around the wet thermometer. The result of the difference in component pressures of the water vapor (air flowing around the wet thermometer) and the ambient air is the evaporation of water from the so-called hygroscopic. The tank with the thermometric liquid cools to the temperature corresponding to the cooling limit [1].

The psychrometric difference is difference between indication of a dry and wet thermometer. It depends on the humidity of ambient air. The lower relative humidity, greater temperature difference. If the air is saturated, namely  $\varphi = 100\%$ , both thermometers will show the same temperature [1].

We use the Sprung formula for psychrometric calculations. It is based on heat taken from the atmosphere used to evaporate the water from wet bulb thermometer. This heat returns in the form of heat of evaporation of water into the air.

With the assumed conditions of heat exchange and free inflow of air mass, knowing the temperatures of thermometers  $t_s$  (dry air temperature) and  $t_m$  (wet air temperature), we can determine the exact air humidity for  $t_s \leq 323,15\text{K}$ , using the Sprung formula [1].

$$\varphi = \frac{p_p}{p''_{ps}} = \frac{p''_{pm-A}(t_s - t_m) \cdot p_b}{p''_{ps}} \cdot 100\%, \quad (1)$$

where:

$$A = \left(65 + \frac{6.75}{w}\right) \cdot 10^{-5} \cdot K^{-1}. \quad (2)$$

A — psychrometric constant dependent on factors such as the type of gas, gas velocity around a container with thermometric liquid thermometer, wet bulb temperature. Psychrometer construction, dimensions and shape of a thermometric liquid container have a very big influence on the psychrometric constant [1].

The Assmann psychrometer is a device consisting of two dry and wet thermometers surrounded by cover (fig. 1). It is additionally equipped with a reservoir with thermometric liquid protection against influence of solar radiation and a fan that generates forced airflow at a speed  $w$  of 2.5 [m/s] to 4.0 [m/s]. This speed corresponds to the psychrometric constant [1, 7].

Measuring range: temperature from 273.15 [K] to 323.15 [K], relative humidity of air from 5 [%] to 95 [%]. If the temperature exceeds  $t_s > 323.15$  [K] then the accuracy decreases. This is due to a non-adiabatic humidification process [11].

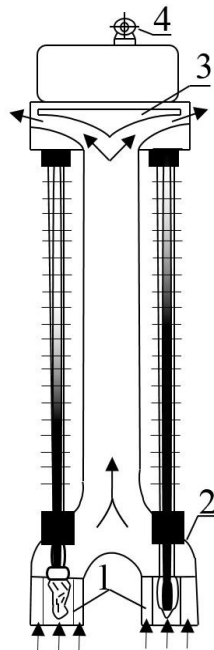


Fig. 1. The Assmann psychrometer [8]:  
 1 — wet thermometer, 2 — dry thermometer, 3 — screens,  
 4 — fan, 5 — fan drive

## THE METHOD OF CALCULATING THE RELATIVE HUMIDITY

The rapid development of microcontrollers was the reason that these systems are increasingly used in various projects, including those related to temperature measurement. Cheap electronic circuits can be used as replacements for expensive components. Projects have already been carried out in which infrared thermometers [5, 6] and microcontrollers [3] were used for hygroscopic measurements. Due to the fact that there is a gap in the availability of simple tools for hygroscopic measurements, authors decided to use DS18B20 digital thermometers for temperature measurement using the Arduino Mega microcontroller system with an LCD display.

### ASPIRATION PSYCHROMETER USING A MICROCONTROLLER SYSTEM

The creation of microcontroller systems forced the appearance of ready devices using these systems. The development of IDE software and libraries has made programming of these electronic components much easier. One of the examples are Arduino systems, which in their design use microcontrollers from the AVR family. The Arduino Mega 2560 R3 was selected for the construction of the psychrometer. The board uses the AVR ATmega 2560 microcontroller. Fig. 2 shows the MEGA2560 R3 board.



Fig. 2. MEGA2560 R3 [9]

Dallas DS18B20 digital thermometers were used to measure the temperature of dry and wet parts. For communication, they use the 1-Wire protocol. Fig. 3 shows the temperature sensor DS18B20. DC electrical characteristics shows tab. 1.

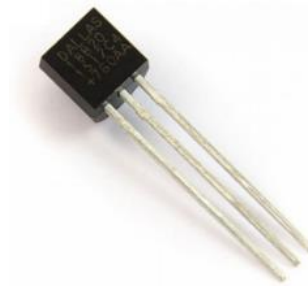


Fig. 3. Digital temperature sensor DS18B20 [10]

Tab. 1. DC electrical characteristics [10]

Parameter	Value
Supply voltage	+3.0 to 5.5 V
Thermometer error	-10°C to +85°C ±0.5°C
	-10°C to +85°C ±1°C
	-55°C to +125°C ±2°C
Input logic-low	-0.3 to +0.8 V
Input logic-high	+3.0 V
Standby current	750 nA
Active current	1.5 mA
Drift	±0.2 °C

To connect sensors of the Arduino board, an intermediate plate was designed in the EAGLE program, on which the digital display, signal diodes, control buttons, pins for 1-Wire communication and a system for controlling the speed of the fan were placed. The diagram of the intermediate plate connections is shown in fig. 4. The plate was made using the thermal transfer method and etched with sodium persulfate.

To make the body of the psychrometer on which the fan was installed, 3D printer was used. For this purpose, a virtual model of the psychrometer was designed in AutoCad program and later the G code was constructed on it. 3D printing was carried out on an IPrus printer. The stand, on which the air flow ducts together with the fan were installed, was made of larch wood. Fig. 5 shows the visualization of the hygrometer model in the AutoCad program.

The system was programmed in the Arduino IDE and mounted on the platform. Fig. 6 shows the complete aspiration psychrometer with the control and measurement system.



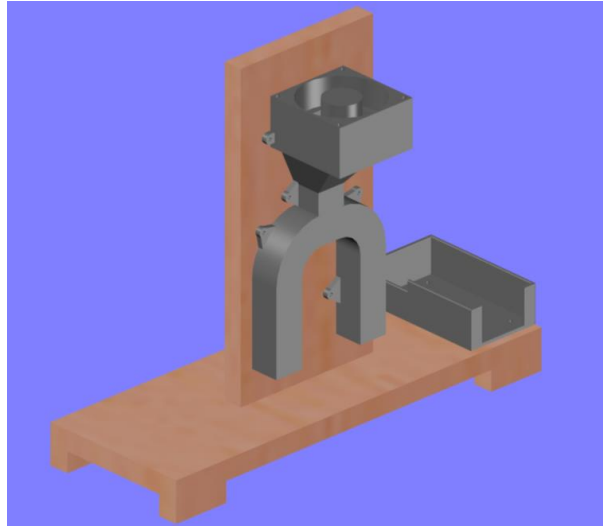


Fig. 5. Visualization of the hygrometer in the AutoCad program



Fig. 6. Aspiration psychrometer based on digital temperature measurement

## RESEARCH AND CALCULATION

The designed aspiration psychrometer was compared with a psychrometer recognized as the model company of 'WSZ Kraków'. The test consisted in measuring the temperature of the 'wet' and 'dry' thermometers of both psychrometers. Eight

measurements were carried out — four under present atmospheric conditions and four using steam produced by an electric kettle. After analyzing the measurement results, the test was presented using tables and diagrams.

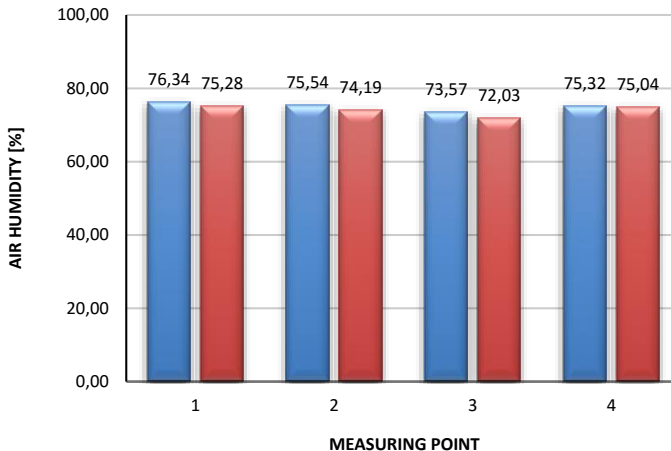


Fig. 7. Comparison of relative humidity under atmospheric conditions: blue — standard psychrometer, red — digital psychrometer

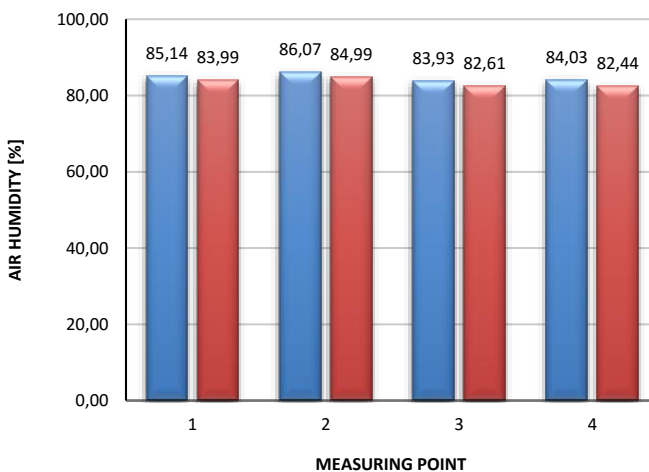


Fig. 8. Comparison of relative humidity in conditions with forced humidity: blue — standard psychrometer, red — digital psychrometer

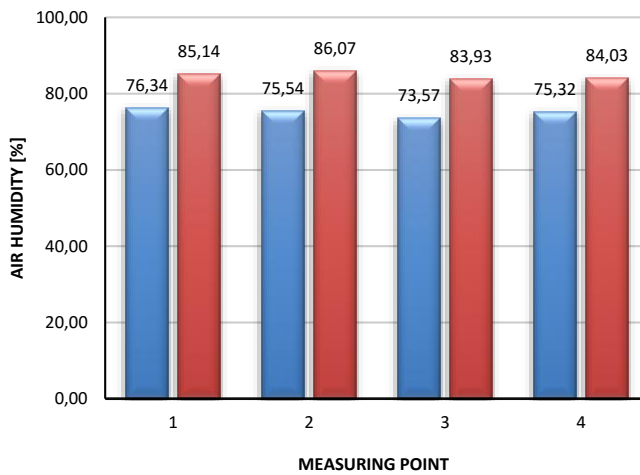


Fig. 9. Comparison of relative humidity under different conditions for the reference psychrometer: blue — standard psychrometer, red — digital psychrometer

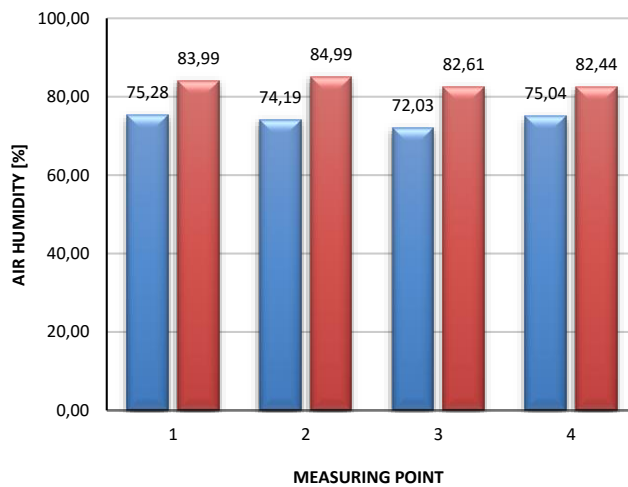


Fig. 10. Comparison of relative humidity in different conditions for digital psychrometer: blue — standard psychrometer, red — digital psychrometer

## CONCLUSIONS

The goal of the project was to build an aspiration hygrometer based on digital temperature measurement. The measurements showed a relative humidity error

not exceeding 2 [%], therefore a hygrometer for lab exercises can be used as a didactic stand.

The temperature results of both psychrometers, which were obtained during measurements under atmospheric conditions, were similar to each other. The relative values calculated on their basis differed from 0.16 [%] to 1.55 [%] depending on the measurement points. Therefore, an arithmetic mean was derived from them, which amounted to 0.69 [%]. This is a favorable result for the digital psychrometer compared to its model counterpart.

In summary, microcontroller systems can be used to build teaching positions. Together with digital sensors that measure to two decimal places, they are an alternative to this type of device.

The position in the future can be equipped with a sensor measuring atmospheric pressure. This would allow a more accurate reading of relative humidity and would improve the work of this device.

## REFERENCES

- [1] Bratek T., Kapitaniak A., Kulesza J. et al., *Pomiary cieplne*, Part 1, Publ. WNT, Warszawa 1993–1995 [*Thermal measurements* — available in Polish].
- [2] Górski J., Matejak M., *Zarys historii pomiaru wilgotności powietrza*, 'Muzealnictwo', 1998, No. 40, pp. 145–150 [*An outline of the history of measuring humidity* — available in Polish].
- [3] Komor G., Nowicki M., Biś K., Szewczyk R., *Microprocessor based assmann psychrometer*, 'Advances in Intelligent Systems and Computing', 2018, Vol. 743, pp. 628–634, DOI: 10.1007/978-3-319-77179-3\_59.
- [4] Kozakiewicz P., Matejak M., *Higrometr — historia pomiaru wilgotności względnej powietrza*, Publ. SGGW, Warszawa 1998 [*History of relative humidity measurement* — available in Polish].
- [5] Lee C., Wang Y. J., *Psychrometer based on a contactless infrared thermometer with a predictive model for water evaporation*, 'Biosystems Engineering', 2017, Vol 160, pp. 84–94, DOI: 10.1016/j.biosystemseng.2017.05.010.
- [6] Li C., Chung J. Y., *A novel design of psychrometer based on a single-packaged contactless infrared thermometer*, 'Journal of Taiwan Agricultural Engineering', 2017.
- [7] Milewska I., Dobrzański T. (ed.), *Mechanik — poradnik techniczny*, Part 3, Publ. PWT, Warszawa 1960 [*Mechanic — technical guide* — available in Polish].
- [8] *Pomiar wilgotności powietrza*, [online], [*Air humidity measurement* — available in Polish], [http://ktc.zut.edu.pl/fileadmin/dydaktyka/instrukcje/cwiczenie\\_9.pdf](http://ktc.zut.edu.pl/fileadmin/dydaktyka/instrukcje/cwiczenie_9.pdf) [access 03.03.2020].
- [9] <https://www.arduino.cc/> [access 03.03.2020].
- [10] <https://www.maximintegrated.com/en.html> [access 03.03.2020].
- [11] [http://www.kseiuos.agh.edu.pl/dla\\_studentow/metrologia\\_cieplna/](http://www.kseiuos.agh.edu.pl/dla_studentow/metrologia_cieplna/) [access 03.03.2020].

## WYKORZYSTANIE MIKROKONTROLERA W BUDOWIE HIGROMETRU ASPIRACYJNEGO

### STRESZCZENIE

W artykule przedstawiono możliwość wykorzystania systemów mikrokontrolerów jako jednego z elementów stanowiska dydaktycznego. Do jego budowy wykorzystano system Arduino Mega oparty na mikrokontrolerze ATmega 2560 z rodziny AVR. W początkowej fazie za pomocą programu AUTOCAD opracowano model higrometru, a następnie wykonano go przy użyciu druku 3D. Po zmontowaniu higrometru przeprowadzono badania z wykorzystaniem opracowanego higrometru oraz higrometru będącego na stanie laboratorium eksploatacji siłowni okrętowych. Badania miały na celu ocenę dokładności opracowanego higrometru. Wyniki badań przedstawiono w końcowej części artykułu.

Słowa kluczowe:

mikrokontroler, higrometr, stanowisko dydaktyczne.

---

*Article history*

Received: 04.03.2020

Reviewed: 23.03.2020

Revised: 28.04.2020

Accepted: 29.04.2020





## MODERN INTEGRATED PLATFORM MANAGEMENT SYSTEM LABORATORY FOR POLISH NAVAL ACADEMY: DESIGN AND IMPLEMENTATION

Rafał Warżala 

*Research and Development Center Maritime Technology Center, A. Dickmana 62 Str., 81-109 Gdynia, Poland; e-mail: rafal.warzala@ctm.gdynia.pl; ORCID ID: 0000-0003-4461-7320*

### ABSTRACT

This article contains a description of the implemented STANTOS™ Integrated Platform Management System (IPMS) laboratory created by Research and Development Center Maritime Technology Center for the Polish Naval Academy in Gdynia. The author briefly described the topology of the solution, justifies the choice of hardware and software solutions. Concept of use was written, where the usefulness of the implemented laboratory was motivated, with a focus on cases where safety plays a key role.

Keywords:

STANTOS, Integrated Platform Management System, IPMS, automation system, maritime.

### Research article

© 2020 Rafał Warżala

This is an open access article licensed under the Creative Commons Attribution-NonCommercial-NoDerivatives 4.0 license (<http://creativecommons.org/licenses/by-nc-nd/4.0/>)

## INTRODUCTION

An Integrated Platform Management System (IPMS) is used on board of naval vessels with automated systems for real-time monitoring and control. A common solution is to control and monitor the status of systems such as propellers, fire-fighting, engines and their support systems, ventilation, fuel, etc. Major manufacturers of industrial automation and ship equipment (such as ABB, Kongsberg, Honeywell) offer such systems. As M. H. Ghaemi describes in his materials: '[...] the factors determining the degree of automation are the result of an economic calculation as well as sociological and psychological considerations. The reason for automation is replacing and simultaneously improving human work, as well as increasing the level of reliability and safety. Automation may be necessary, especially when it comes to automatic regulation, cooperation with the superior system, quick processing of a large amount of information or optimization of the engine's operation. Ultimately, automation results in a reduction of crew size' [1]. Often, the degree of automation is imposed by the classification environment or the shipowner's requirements [6]. Despite the increasing degree of automation and the reduction in the number of crew (accompanied by an increase in its competence) is essential. Assuming that the faster a crewman acquires knowledge and skills, the better it is, naval school would be the optimal place to gain these abilities. Naval Academy in Gdynia states that its graduates will be prepared to make operational decisions in difficult, maritime conditions concerning the use of vessel's power plant, as well as in extreme combat conditions. Graduates will also have qualifications covering knowledge of operation and operation of propulsion [8]. An academy preparing students for work at sea should consider that nearly half of accidents at sea are caused by the human factor [12]. The Academy, aware of the importance of proper crew training on simulators, decided to create an IPMS laboratory. Ośrodek Badawczo-Rozwojowy Centrum Techniki Morskiej S.A. — OBR CTM S.A. (Research and Development Center Maritime Technology Center) responded to this demand by proposing the implementation of its STANTOS™ System. The STANTOS™ Software is a modern SCADA (Supervisory Control And Data Acquisition) system that supervises the operation of ship systems. Its tasks include presenting current and archival measurements of ship system sensors as well as alarm signals. The system performs all functions of alarm and control, data management, displaying event history logs and allows to create independent applications that manage industrial automation. The basic

design assumption was to enable simulation of a real, modern platform management system. STANTOS™ consists of elements used to simulate the technical and software components of IPMS systems. While working on a dedicated solution, SIMATIC tool and Inkscape SAGE licensed commercial software were used. This system enables the set up and modification of hardware and software configuration to achieve the required teaching objectives related to both the design of marine IPMS systems as well as their technical support (supervision and repairs). Actuators are simulated in the software and modelled in the hardware layer by using a number of basic automation components. This allows the Academy to provide courses on a very wide range of topics: from the design and implementation of basic IPMS subsystems, through connecting subsystems into a network, to the operation of a simulated IPMS system [4]. In the next section design of laboratory is presented. Then, the hardware and software solution is shown and at the end concept of use was described.

## **DESIGN**

The main advantages of distributed systems are such features as: role distribution, resource sparing, system reliability, process concurrency, scalability and fault tolerance [5]. Therefore, it was decided to implement the automation system in a distributed type. Fig. 1 shows system topology.

Each automation workstation is responsible for a dedicated ship system and connected together in architecture based on the Ethernet ring topology. Architecture of this type has an increased resistance to failures, which allows for efficient operation of the system even after malfunction or damage to some of its elements, e.g. cables or network switches. STANTOS™ has a modular structure, giving the possibility of easy configuration of software and hardware components building appropriate functionalities dedicated to specific customer needs. The software is based on the universal SEFCOM (Sensor Effector Communicator) framework, which is the basis of other ship systems implemented by OBR CTM S.A. (Research and Development Center Maritime Technology Center).

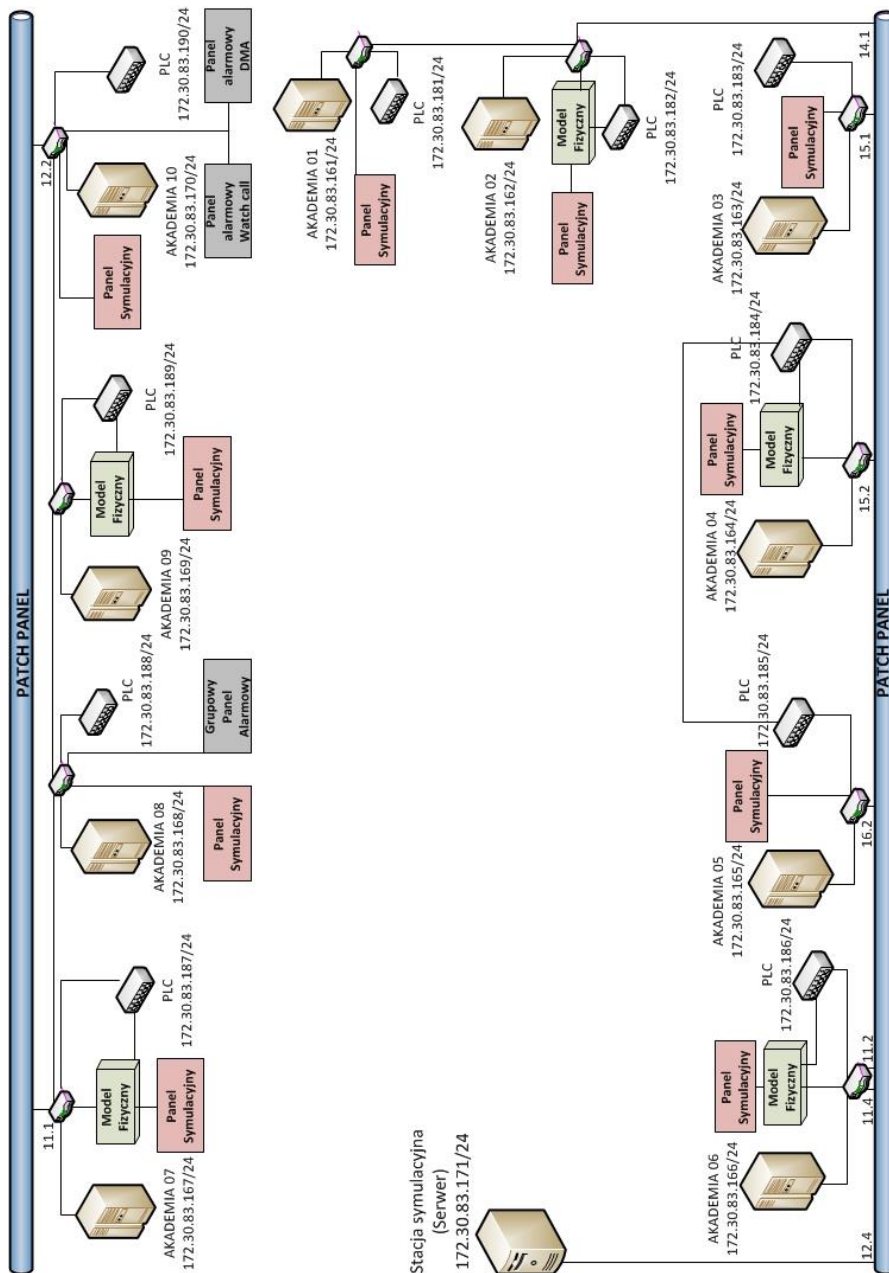


Fig. 1. STANTOS™ System topology consisting of blocks: panel symulacyjny (Simulation Console), model fizyczny (Physical Model), grupowy panel alarmowy (Group Alarm Panel), panel alarmowy Watch Call (Watch Call Alarm Panel), panel alarmowy DMA (Dead Man Alarm Panel), stacja symulacyjna (Simulation Station) [4]

## HARDWARE

The STANTOS™ System consists of the following components (fig. 1): 10 Workstations with STANTOS™ Software, 10 Simulation Panels, 10 PLC Controllers, 5 Physical Models, 1 Simulation Station (STANTOS™ Server), 1 'Deadman' Alarm Panel, 1 'Watch Call' Alarm Panel, 1 Group Alarm. Each of the 10 laboratory stations is equipped with an automation set (fig. 2). All elements of automation are connected with each other by a fast, industrial automation network, allowing mutual communication.

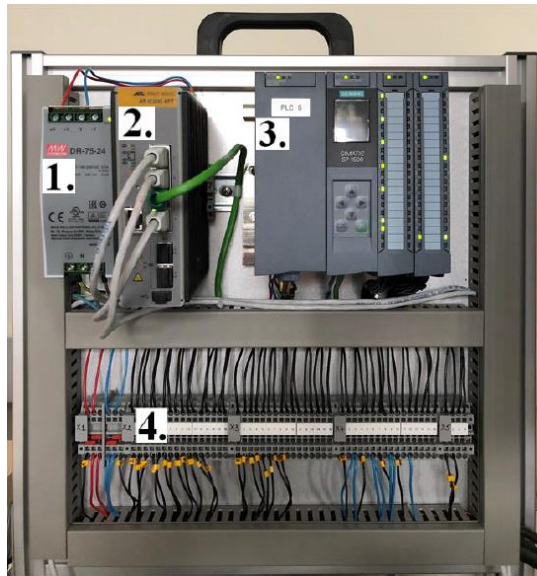


Fig. 2. Photo of rack with automation set where:  
1. Power Supply, 2. Switch, 3. PLC S7-1500, 4. Junction Strips [4]

PLC Controllers can be programmed to work with Physical Models and Simulation Panels using the SIMATIC tool software. Physical Models are a mapping of real ship systems, but they are simplified representations in the scope that allows to understand the mechanisms of system operation and to conduct laboratory exercises. Physical Models generate appropriate signals, which after processing by PLC Controllers are received by the STANTOS™ System and visualized as events of real ship systems. Physical Models respond to control signals generated from Workstations. The set of Physical Models represents 5 different ship systems: ballast, ventilation, fuel, fire-fighting and oil.

Simulation Panels are devices that generates simple digital and analogue signals for simulating signals from marine equipment and systems. These signals are received by I/O modules of PLC Controllers and processed for presentation in SCADA software or STANTOS™ System as signals of real devices.



Fig. 3. Photo of Simulation Panel [4]

Simulation Panels (fig. 3) by working in a shared network can present events simulated by the Simulation Station or events developed by other laboratory stations using their own simulation panel.

The Deadman Alarm (DMA) panel is used to monitor and supervise the presence of machine personnel in the ship's power plant in unattended operation mode. The appearance of the 'Deadman Alarm' alarm panel is shown in fig. 4 and 5 shows an example of a commercial DMA panel.



Fig. 4. Photo of Deadman Alarm Panel [4]



Fig. 5. Photo of commercial DMA panel [10]

The Group Alarm Panel is used to signal alarm states from selected Alarm Groups. This panel is equipped with lights signalling an alarm. Panels of this type are usually placed in the navigation cabin and the ship's engine control centre. Figures presented below compare a Group Alarm Panel made by OBR CTM S.A. and a commercial version.

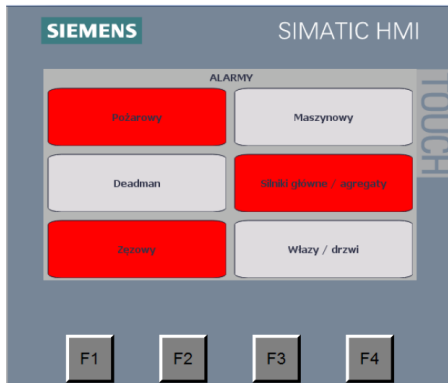


Fig. 6. Photo of Group Alarm Panel [4]



Fig. 7. Photo of Commercial Group Alarm Panel [9]

The Watch Call System is designed to inform the watch mechanic about the occurrence of an alarm condition or warnings. Panels of this type are usually placed in social rooms (e.g. a mess room) and in the crew quarters. Fig. 8 and 9 present a Call Panel made by OBR CTM S.A. and a commercial version.

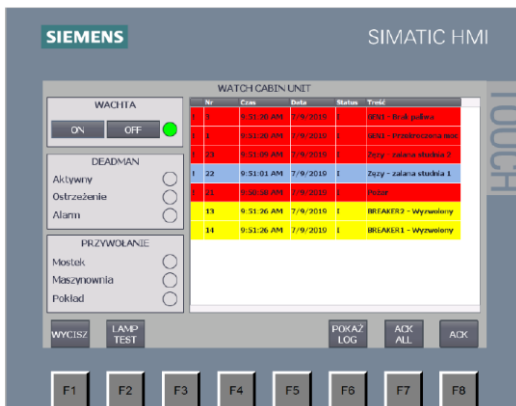


Fig. 8. Photo of Watch Call Panel [4]



Fig. 9. Photo of commercial Watch Call Panel [11]

## SOFTWARE

In addition to the STANTOS™ Software, Inkscape SAGE has been installed on each operator console. Inkscape SAGE is a powerful tool for designing and visualizing software components. The design version allows an efficient design of advanced applications and has the necessary symbols library designed to create perspectives in the field of industrial and process automation. User can also expand STANTOS™ with new perspectives or elements. It is also possible for the user to create his own applications.

Each of 10 PC workstations with STANTOS™ Software has an Ethernet connection with the simulation station. Exchange of information between them is possible through a STANTOS™ Server located at the simulation station. To ensure reliable operation and continuous synchronization between system components, the Network Time Protocol is employed. A simulation station is also used as a time server which periodically provides time synchronization in the system with a period of one minute.

To provide the scalability of the project and efficiency of data exchange between consoles and PLC (through the STANTOS™ Server) it was decided to use the OPC UA protocol. An OPC server has been activated on each of the 10 PLCs. STANTOS™ Communicator is a client for these servers and is a type of a 'translator' of protocol for the server. STANTOS™ Simulator perspective is shown in fig. 10.

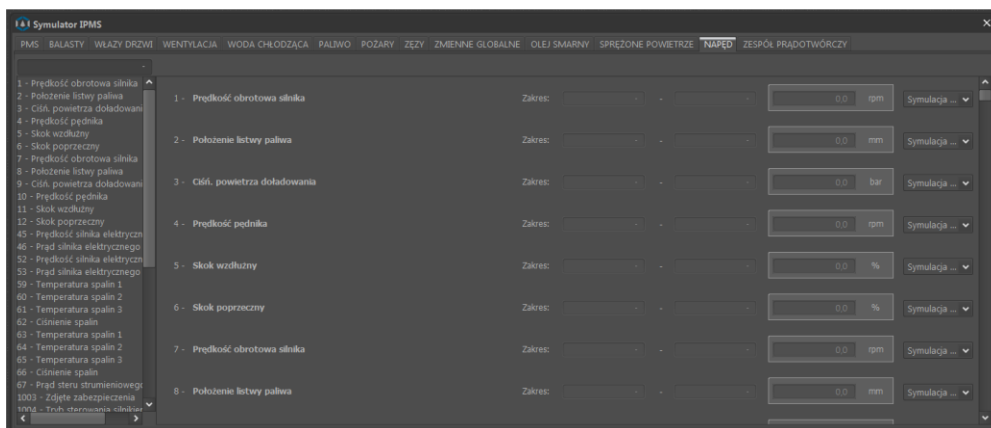


Fig. 10. STANTOS™ Simulator view [4]

The simulator software, which is located on the simulation station, performs all simulation and training functions of the Integrated Platform Management System. Alarm events of simulated ship devices are generated at the Simulation Station. Both analogue and digital values of simulated sensors and measuring devices can be set.

After launching the STANTOS™ Application on the operator's console and logging in, a navigation panel will appear to move between perspectives. In addition to the System and Trends tab, each perspective corresponds to individual systems simulated for the needs of the laboratory.

## CONCEPT OF USE

The efficiency of the engine room is critical to the ship's manoeuvrability. Losing it may lead to losses due to the destruction of the vessel and port infrastructure. What might be the consequences of a blackout on a ship is shown in the MV Planet V case study, where one of the sailors lost his life [2]. As Damir Radan proves in his doctoral dissertation: Power Management System interacts with the propellers by the following functions: available power static load control, load rate limiting control and blackout prevention control. These functions serve to prevent the blackout and to ensure that the vessel will always have enough power available [7]. In the STANTOS™ System, the power supply system has been modelled as a central energy distribution system. Energy from two generators is transferred directly to the main switchboard. The main switchboard is divided into two sections connected by bus-tie (breaker connecting electric bars between sections). Electrical supply perspective is shown in fig. 11.

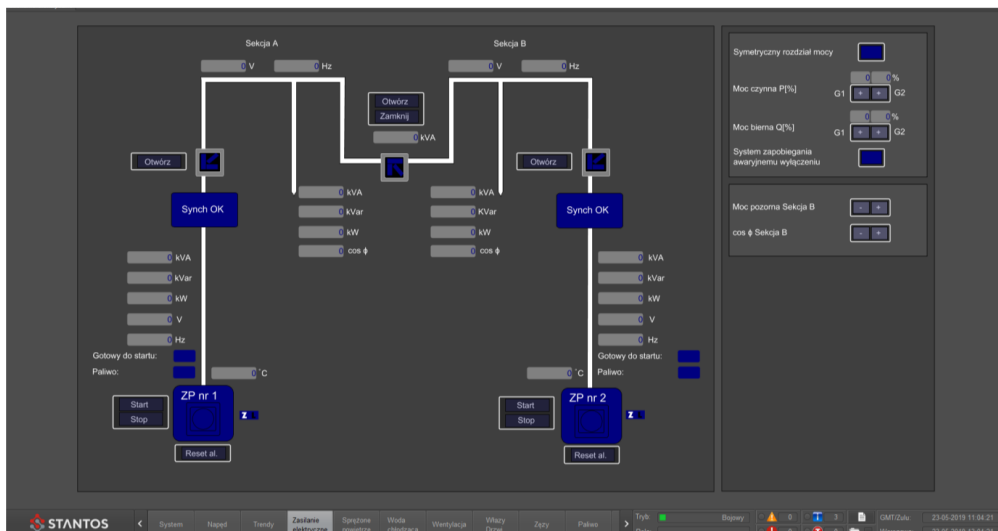


Fig. 11. View at Power Supply Perspective [4]

STANTOS™, as a useful teaching tool, enables the student to get acquainted with the work of the Power Management System. In the event of a system failure one can find in Trends tab what were the parameters of individual elements of the system at any given time instance, and there is an information of active warnings and alarms and a log of their history on the alarm panel. This allows to gain experience with dealing with this kind of failures and to train one in correctly diagnosing the system. Among other functionality, it is possible to simulate the running after blackout, automatic and manual synchronization of individual generating sets. Using STANTOS™, the student will learn how to avoid blackout and practice the correct sequence of activities needed to be performed.

Raising the degree of vessel's functions automation positively affects the sociological aspect of crew work comfort. However, it should be remembered that safety is a priority in the maritime industry. That is why classification environments allow for unattended operation of the machinery, but this matter is secured with many specific restrictions [3, 6]. One of these requirements is to provide detection of increasing of level of water in the engine room bilges or bilge wells. The student can simulate the flooding of wells to get the experience of handling in case of such situation occurring on the vessel.

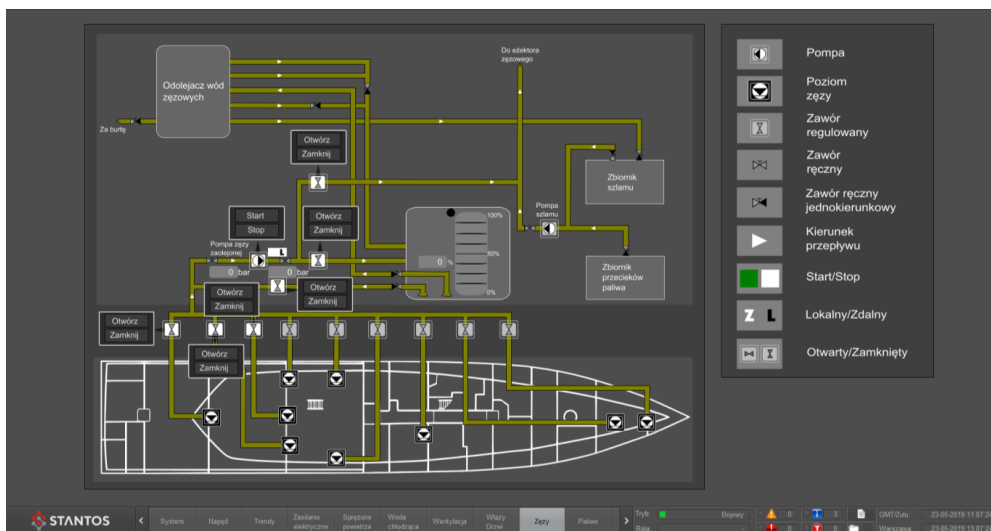


Fig. 12. View at Bilge Perspective [4]

Another classification environment safety requirement that directly affects human health and life is the operation of the Dead Man / Patrol Man System. Lloyd's

requires the alarm system to be reset at predetermined intervals (e.g. each 30 minutes) [3]. If the Dead Man panel is active and there is no reset after the set time interval, an alarm will be signalled locally. Information about the warning and the alarm will also appear on the alarm panel. Using this system in the laboratory will allow the student to develop the habit of taking care of his own safety by using devices and systems serving this purpose.

## CONCLUSIONS

The project of the IPMS system, its design solutions and the justification for the chosen topology were described in this article. Selection of hardware was first determined by its educational value. Other objectives were to allow to sustain scalability of hardware and provide possibilities to expand project. The main goal of using STANTOS™ is education, becoming familiar with the principles of IPMS and to gain proper habits, especially in emergency situations. Moreover, the functional use aspect of the application's operation was maintained — data is read from real sensors, and real actuators are activated. The software used here allows the student to become familiar with the graphic interface used by OBR CTM S.A. in other products, such as Combat Management Systems. Laboratory project was design as open-source type of educational tool. This system can be expanded for example by a graduating student during his diploma thesis. One particular area of future development is the integration with other Academy laboratories, allowing to exchange data between them. This system has great educational value, supporting students in understanding bigger systems and processes.

## Acknowledgments

Laboratory was made by Ośrodek Badawczo-Rozwojowy Centrum Techniki Morskiej S.A. (Research and Development Center Maritime Technology Center).

## REFERENCES

- [1] Ghaemi M. H., *Podstawy automatyzacji okrętu. Techniczne, ekonomiczne i socjologiczne aspekty automatyzacji okrętu*, Gdańsk 2018 [*Ship autopation basics. Technical, economic and sociological aspects of ship automation* — available in Polish].

- [2] Hasegawa K., Ibn Awal Z., *Analysis of Ship Accidents due to Marine Engine Failure — Application of Logic Programming Technique*, 'Journal of the JIME', 2015, Vol. 50, No. 6, pp. 40–46.
- [3] Jong I. W. de, *Machinery Alarm Systems for Ships Operated with Unattended Machinery Spaces*, Lloyd's Register of Shipping, Rotterdam 1973.
- [4] *Laboratorium IPMS Akademii Marynarki Wojennej. Instrukcja użytkowania oprogramowania STANTOS™*, Research and Development Center Maritime Technology Center, 2019 [*IPMS Laboratory of the Naval Academy. STANTOS™ Software user manual* — available in Polish].
- [5] Mosorow W., *Systemy rozproszone*, Lodz University of Technology, Łódź, 2007 [*Distributed systems* — available in Polish].
- [6] *Przepisy klasyfikacji i budowy okrętów wojennych, cz. VIII, Instalacje elektryczne i systemy sterowania*, Polski Rejestr Statków, Gdańsk 2008 [*Standards for the classification and construction of warships, Part VIII, Electrical installations and control systems* — available in Polish].
- [7] Radan D., *Integrated Control of Marine Electrical Power Systems*, PhD Thesis, Norwegian University of Science and Technology, Trondheim 2008.
- [8] *Sylwetka absolwenta wojskowego*, [online], <http://www.wme.amw.gdynia.pl/dla-studentow/sylwetka-absolwenta/sylwetka-absolwenta-wojskowego> [access 05.01.2020], [*Military graduate profile* — available in Polish].
- [9] Website 'Böning Automationstechnologie GmbH & Co. KG', [online], [https://www.boening.com/ahd\\_406-2.html?&L=1](https://www.boening.com/ahd_406-2.html?&L=1) [access 05.01.2020].
- [10] Website 'Pan Delta Controls PTE LTD', [online], <https://www.pandelta.com/> [access 05.01.2020].
- [11] Website 'Ship automation', [online], <https://www.shipautomation.com/product/kongsberg-watch-cabin-unit-display/> [access 05.01.2020].
- [12] *Wypadki i incydenty morskie. Roczna analiza*, State Marine Accident Investigation Commission, 2017 [*Marine accidents and incidents. Annual analysis* — available in Polish].

## **NOWCZESNE LABORATORIUM ZINTEGROWANEGO SYSTEMU ZARZĄDZANIA PLATFORMĄ DLA POLSKIEJ AKADEMII MARYNARKI WOJENNEJ: PROJEKT I WDROŻENIE**

### **STRESZCZENIE**

Artykuł zawiera opis wdrożonego laboratorium zintegrowanego systemu zarządzania platformą (IPMS) STANTOS™ stworzonego przez Ośrodek Badawczo-Rozwojowy Centrum Techniki Morskiej S.A. dla Akademii Marynarki Wojennej w Gdyni. Autor krótko opisał topologię rozwiązania, uzasadniając wybór rozwiązań sprzętowych i programowych. Napisano koncepcję użytkowania,

w której uzasadniano przydatność wdrożonego laboratorium, ze szczególnym uwzględnieniem przypadków, w których bezpieczeństwo odgrywa kluczową rolę.

Słowa kluczowe:

STANTOS, zintegrowany system zarządzania platformą, IPMS, system automatyki, technika morska.

---

*Article history*

Received: 01.03.2020

Reviewed: 24.04.2020

Revised: 13.05.2020

Accepted: 05.06.2020





## A CONCEPT OF BLDC DRIVE MODEL CONTAINING BATTERY CELL MODEL

Michał Brodzicki<sup>1</sup>, Przemysław Chrabąszcz<sup>2</sup>

*Polish Naval Academy, Faculty of Mechanical and Electrical Engineering, Śmidowicza 69 Str., 81-127 Gdynia, Poland; e-mail: m.brodzicki@amw.gdynia.pl, p.chrabaszcz@amw.gdynia.pl; ORCID ID: <sup>1</sup>0000-0002-0366-6292, <sup>2</sup>0000-0003-0196-957X*

### ABSTRACT

The paper presents a concept of overall BLDC drive model. Target model will be improved with a functional model of battery cell, which is commonly used as a power supply for the drive. The paper shows previous achievements in form of a functional BLDC motor model. Also, simulation results are presented. These are the partial results, that aimed to verify the basic model's correctness as a basis of future developments. The procedure of power source selection presented in the article is vital to specify the technical parameters of modelled battery cell.

#### Keywords:

BLDC drive, electrical drives, electrical machines, hybrid power source, li-Ion batteries, supercapacitors.

#### Research article

© 2020 Michał Brodzicki, Przemysław Chrabąszcz  
This is an open access article licensed under the Creative Commons  
Attribution-NonCommercial-NoDerivatives 4.0 license  
(<http://creativecommons.org/licenses/by-nc-nd/4.0/>)

### INTRODUCTION

BLDC (Brushless Direct Current) motor is a specific type of electrical machines, which is currently commonly used as a propulsion for many electrical vehicles. BLDC is in fact a combination of PMSM (Permanent Magnet Synchronous Machine) motor and an electronic device responsible for steering and powering up the motor. The typical structure of BLDC drive is presented in fig. 1.

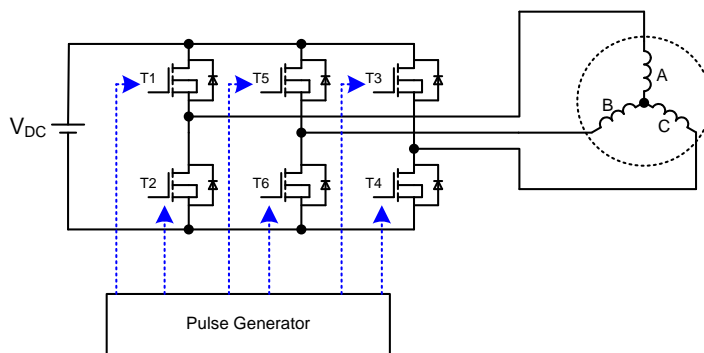


Fig. 1. Typical structure of BLDC motor [4, 6]

PMSM motor itself is an AC machine, but as a consequence of electronic device application it can become a DC machine. This electronic device is an electronic controller, which can be considered as a commutator for the motor. The controller generates voltages that power up the motor. Generated voltages are square-type and are called the commutator functions, shown in the fig. 2 [2, 4, 6].

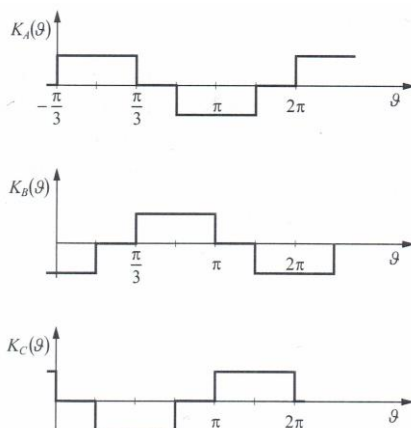


Fig. 2. Commutator functions for each BLDC motor phase [2]

The controller has a bridge structure and is based on MOSFET transistors, which are controlled with externally generated pulses. PWM algorithm was not used in this basic model, but general concept allows its implementation. Consequently, voltages in the motor phases are specifically shaped, what affects the shape of EMF induced in motor's windings. EMFs in BLDC motors are typically sinusoidal or trapezoidal [1, 3, 5].

### SIMULATION MODEL OF BLDC MOTOR

The model of BLDC motor was developed in Matlab/Simulink using pre-defined function block, which is an implementation of PMSM motor's mathematical model. The block was modified with specific values of windings' resistance and inductance along with mechanical parameters. Fig. 3 illustrates the final structure of the BLDC model.

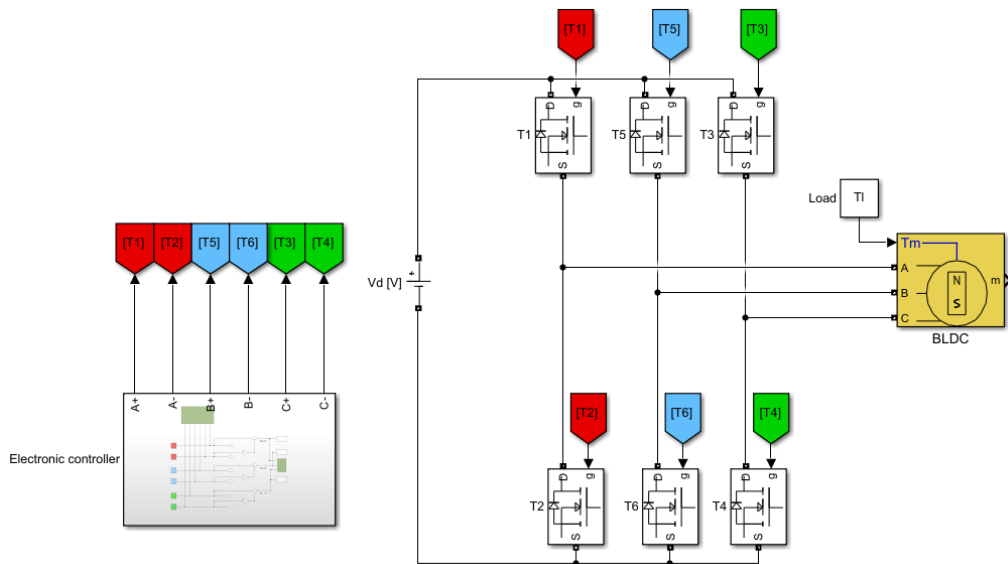


Fig. 3. Schematic BLDC motor model

The model represents a BLDC motor described with rated parameters shown in tab. 1.

Tab. 1. Rated parameters of the modelled BLDC motor

Parameter	Unit	Value
Rated power	W	1000
Rated voltage	V	35–45
Rated speed	RPM	3000
Rated torque	Nm	3

The electronic controller model was developed individually using pre-defined blocks modelling MOSFET transistors. This represents the classic solution of electronic controller, while modern controllers are based on IGBT transistors. The model is a three-phase bridge powered by DC voltage source. Each transistor valve is switched with individual pulses generated externally. As a consequence, the voltages generated by the controlled are bipolar pulses, that fill the commutator functions presented in fig. 2.

Whole model is combined with external file carrying the code for the simulation. Parameter definition and variables declaration is also done within the mentioned file. This solution allows parameters' modifications or non-complicated simulations' scenarios definition. What is more, the structural model can be also easily implemented to different BLDC motors parametrized with Matlab code files.

### SIMULATION RESULTS

The developed BLDC motor's model was tested during a typical starting simulation. The scenario represented a start of a nominally loaded motor from zero to its rated speed. Simulation results are shown in fig. 4 and 5.

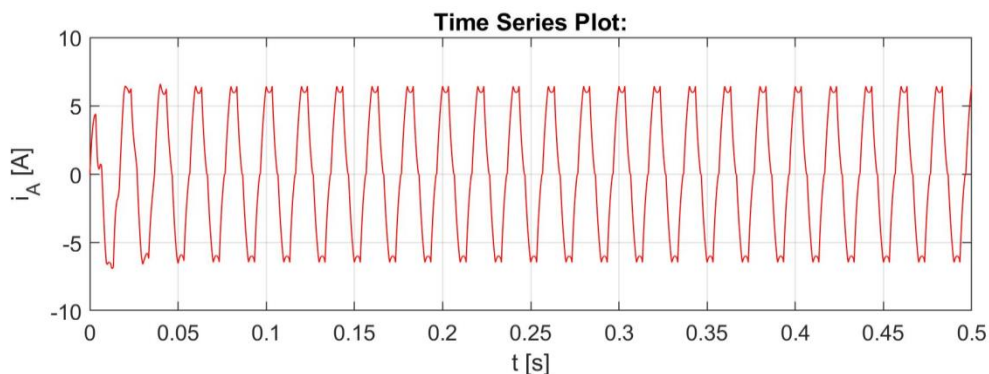


Fig. 4a. Illustration of motor current waveforms — phase A

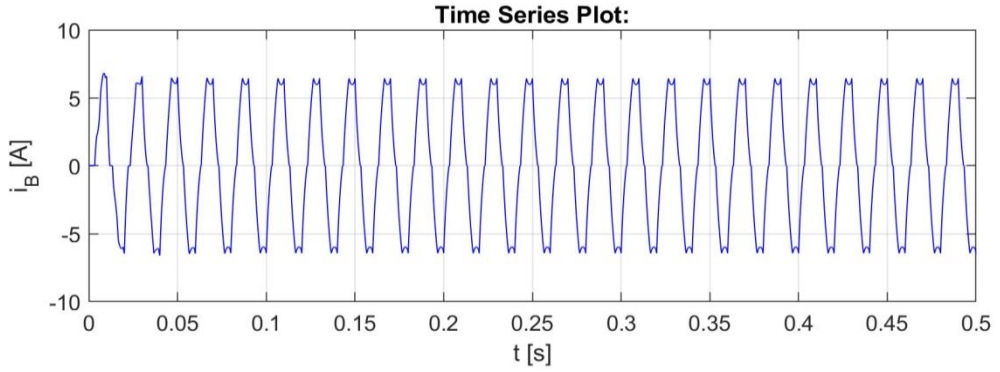


Fig. 4b. Illustration of motor current waveforms — phase B

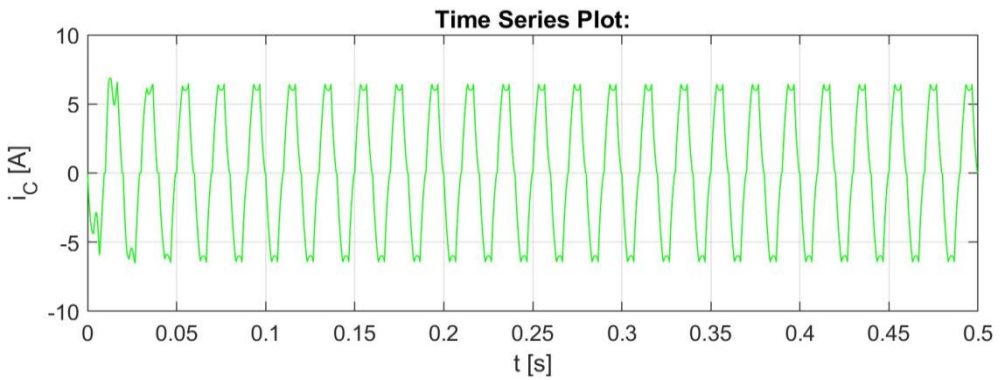


Fig. 4c. Illustration of motor current waveforms — phase C

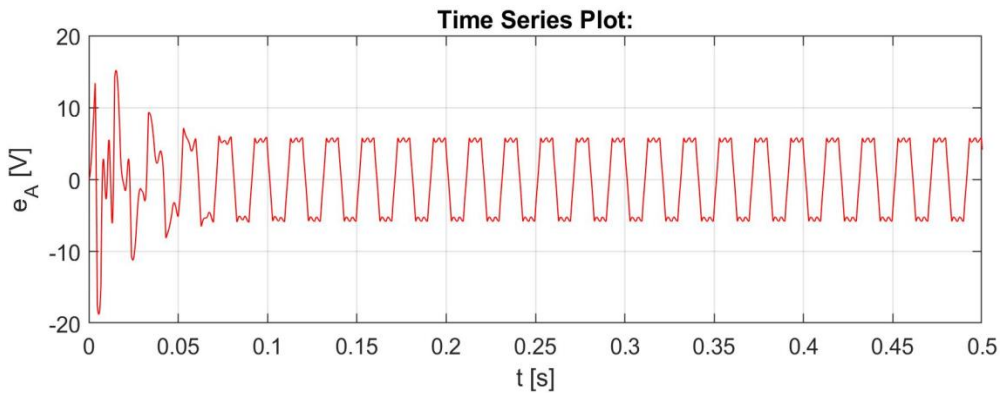


Fig. 5a. Illustration of motor EMF waveforms — phase A

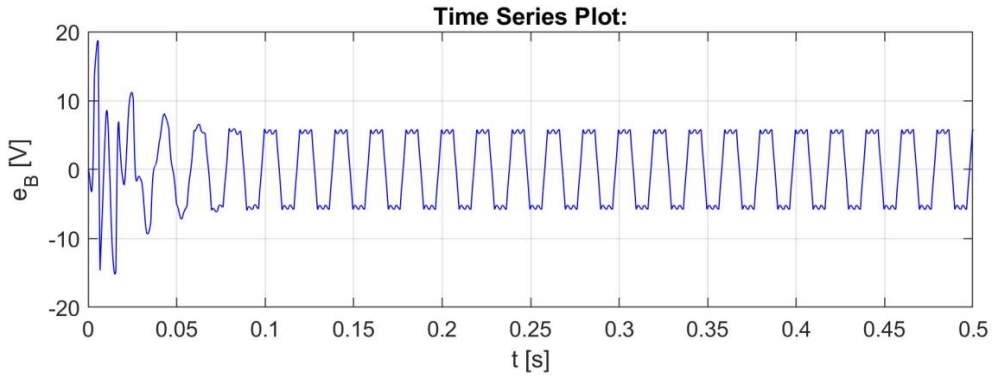


Fig. 5b. Illustration of motor EMF waveforms — phase B

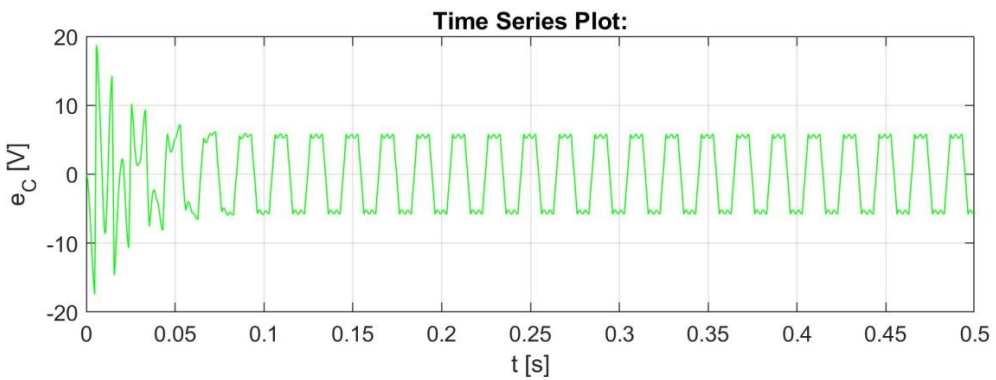


Fig. 5c. Illustration of motor EMF waveforms — phase C

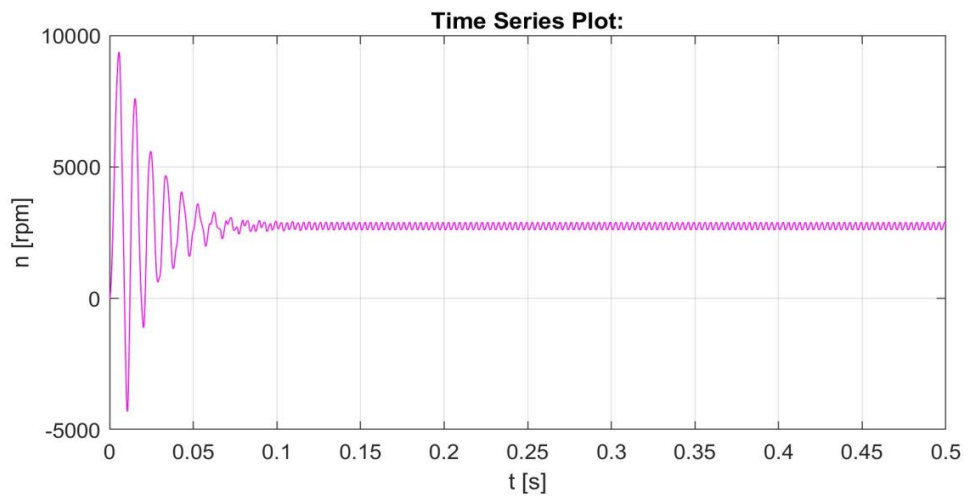


Fig. 6. Illustration of motor speed

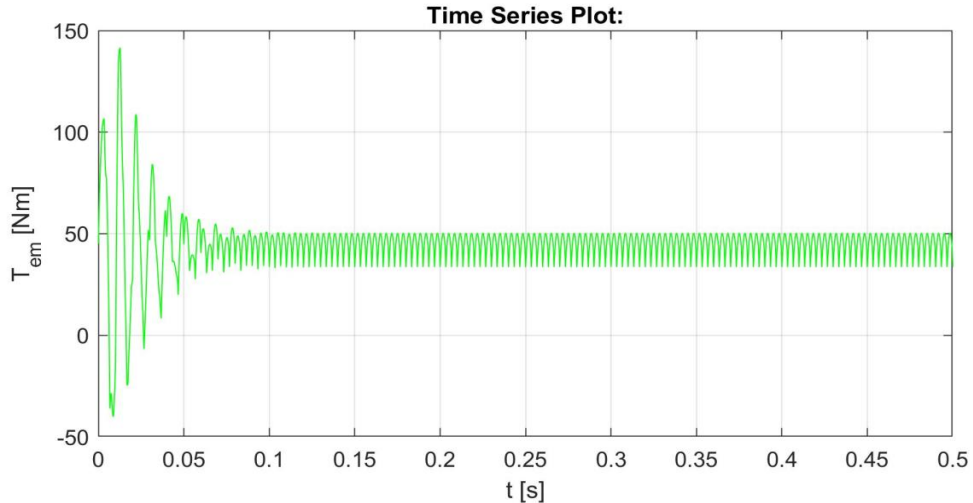


Fig. 7. Illustration of motor electromagnetic torque

Simulation results show, that model fulfils the assumptions. After short-time dynamic state the motor reaches its steady-state operating point. EMFs and currents stabilise and change periodically as a consequence of controller switching. Phase EMFs are trapezoidal what meets the assumption of trapezoidal shape. Result values derive from the model parameters and simulation scenario. Although the motor loading is equal to motor's rated torque, the drive starts as predicted and its further operation is stable.

All the resulting curves are bipolar, which is also a consequence of initial assumptions. All these facts show, that both the PMSM motor and controller models work correctly and represent the BLDC motor acceptably. Concluding, described basic BLDC model can be approved as a basis for further analysis and improvements. However, it is currently powered with ideal DC voltage sources, which is not affected by the drive itself. As a consequence, a specific scope of impacts is omitted. Thus, the model's crucial improvement should be the implementation of battery cell model as a power source for the whole BLDC drive.

## HYBRID POWER SOURCE — CONSTRUCTION GUIDELINES

For the model of the engine adopted for the simulation, an energy storage should be designed in the form of a hybrid power source. The desired effect is planned to be achieved by combining electric energy sources in the form of batteries and

supercapacitors in a way that allows their advantages to be used while minimizing the disadvantages and meeting the energy balance conditions.

As a result, tables were prepared with the outcomes of the preliminary calculations for power elements. That data will allow to determine the minimal number of key power source elements to achieve required nominal power. What's more, summaries of various technical parameters can be a source of data relevant to the prototype design of the device. At the stages of further development of the project, there may be a need to increase the drive power, and hence the efficiency of the source. Therefore, in order to obtain a comparative scale, it was included in calculations.

### THE HYBRID POWER SUPPLY CONCEPT

In order to ensure uninterrupted high quality power supply, especially in situations of momentary high power demand (rapid acceleration, reversing), the galvanic cell battery will be supported by a supercapacitors modules (fig. 6). Due to the complexity of the charging and discharging control processes, the Battery Management System (BMS) must be applied. Widely available li-Ion chemical cells grouped in series packages of ten items (10S) were taken into consideration.

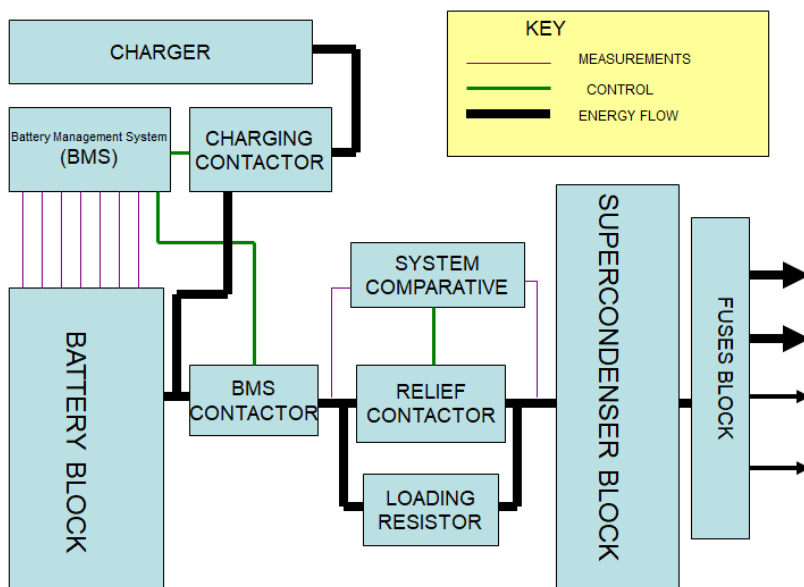


Fig. 6. Schematic diagram of a hybrid power source with protections (own studies and drawings P. Chrabąszcz)

## PRELIMINARY PARAMETERS OF THE POWER SUPPLY SYSTEM PROJECT — ASSUMPTIONS

1. The main energy receiver will be a 1kW brushless electric motor powered by an electronic adapter.
2. The electric motor works at constant speed (speed stabilization) — the power drawn from the source is constant.
3. The bottom catalogue value was used as the battery voltage level.
4. Calculations were made for packs of serially combined batteries of 10, based on data from catalogue cards.
5. To determine the volume occupied by cylindrical cells it was assumed that they are cuboids.

### SELECTION OF THE NUMBER OF BATTERY CELL PACKAGES

Preliminary calculations were made based on cell manufacturers' data [8, 9]. The obtained results allow to determine the extreme parameters of the constructed power source, including:

- the minimum impassable number of cells of a given type necessary to supply a specific power to the drive, meeting the condition of maximum current carrying capacity of each cell;
- minimal system operational times;
- mass and volume of the packages — allowing to determine the amount of space needed.

Tab. 2 and 3 present a summary of the parameters used in further analysis. The parameters in tab. 3 were calculated for 10S packages.

Tab. 2. Input values for calculations of analysed cells [8, 9]  
(own studies and calculations P. Chrabąszcz)

Cell type	Maximum discharge current [A]	Maximum charging current [A]	Nominal Capacity [Ah]	Cell volume [cm <sup>3</sup> ]	Cell weight [g]	Minimum operating voltage [V]	Nominal voltage [V]
NCR 18650GA	10	1.675	3.45	23.826	49.5	2.5	3.6
ICR 18650-26A	5.2	2.6	2.6	23.826	47	2.75	3.7

Tab. 3. Input values for calculations of analysed 10S cell packs [8, 9]  
(own studies and calculations P. Chrabąszcz)

Cell type	Nominal operating voltage of the packet 10S [V]	Minimum packet operating voltage 10S [V]	Maximum working voltage of the 10S packet (after charging) [V]
NCR 18650GA	36	25	42
ICR 18650-26A	37	27.5	42

Based on the preliminary data from tab. 2 and 3, power packs were calculated for the most adverse operating conditions — near-discharge packs. In addition, calculations were made regarding the number of cells necessary for an adequately longer operational time of the source with a given input power. The results are shown in tab. 4–7.

Tab. 4. Extreme values for designing a hybrid power source for 10S NCR 18650GA battery cells for the minimum possible operating voltage of 25V resulting from the maximum current carrying capacity of each cell (own studies and calculations P. Chrabąszcz)

Maximum continuous drive power consumption [kW]	Maximum current consumption [A]	Minimal number of cell packs 10S parallel [pcs]	Package capacity [Ah]	Maximum working time with rated power [h]	Maximum charging current [A]	Minimal charging time [h]	Volume of the whole packet [cm <sup>3</sup> ]	Total weight of the packet [kg]
1	40	4	13.8	0.35	6.70	2.06	953	1.98
2	80	8	27.6	0.35	13.40	2.06	1906	3.96
4	160	16	55.2	0.35	26.80	2.06	3812	7.92

Tab. 5. The minimum total number of 10S cell packages of the NCR 18650GA type for a given operating time at a specific constant power consumption (own studies and calculations P. Chrabąszcz)

Maximum continuous drive power consumption [kW]	1h [number of sets 10s]	2h [number of sets 10s]	3h [number of sets 10s]	4h [number of sets 10s]
1	12	23	35	46
2	23	46	70	93
4	46	93	139	186

Tab. 6. Extreme values for designing a hybrid power source for ICR 18650-26A batteries for a minimum operating voltage of 27.5 V resulting from the maximum current carrying capacity of each cell (own studies and calculations P. Chrabąszcz)

Maximum continuous drive power consumption [kW]	Maximum current consumption [A]	Minimal number of cell packs 10S paralell [pcs]	Package capacity [Ah]	Maximum working time with rated power [h]	Maximum charging current [A]	Minimal charging time [h]	Volume of the whole package [cm <sup>3</sup> ]	Total weight of the package [kg]
1	36.36	7	18.18	0.50	18.18	1.00	1666.15	3.29
2	72.73	14	36.36	0.50	36.36	1.00	3332.31	6.57
4	145.45	28	72.73	0.50	72.73	1.00	6664.62	13.15

Tab. 7. The minimal total number of 10S ICR 18650-26A cell packages for a given operational time at a specified constant power consumption (own studies and calculations P. Chrabąszcz)

Maximum continuous drive power consumption [kW]	1h [number of sets 10S]	2h 1h [number of sets 10S]	3h1h [number of sets 10S]	4h1h [number of sets 10S]
1	14	28	42	56
2	28	56	84	112
4	56	112	168	224

While selecting devices powered from the hybrid power source, one should take into account the wide voltage range of the battery (36–42V), resulting from the voltage characteristics of Li-Ion cells [8] (own studies, drawings and calculations P. Chrabąszcz).

### SELECTION OF SUPERCONDENSORS FOR HYBRID POWER SUPPLY — PRELIMINARY CALCULATIONS

Knowing the maximum currents taken from the Li-Ion cell battery and the maximum operating voltage of the power source, it is possible to select supercapacitors for the hybrid power source. The role of capacity in this system is to reduce

the chemical cell load at peak and momentary consumption, thanks to which the nominal currents can be taken in the calculations, and then in the BCM settings. The input parameter in the designed system will be the maximum cell ampacity.

Peak currents were assumed — in the form of short-term pulses (not longer than 5s) at the level of 150% of the rated current. Single supercapacitors are available for low supply voltages. Importantly, exceeding the low allowable operational voltage of individual cells can cause their damage with further effects. In order to obtain higher operating voltages, supercapacitors are connected in series, at the expense of a decrease in their capacity. As a result of the occurrence of the leakage phenomenon, unequal distribution of voltages on individual cells may occur, and eventually some of them may be damaged. To prevent this, special voltage equalization systems, called balancers, should be used. Supercapacitors are characterized by equivalent series resistance (ESR), which defines their ability to quickly accumulate and give off energy. While the phenomenon of rapid energy release is beneficial for our power source, as it compensates for the momentary rapid demand of loads, the speed of energy storage is not. After parallel connection of the supercapacitors package to the accumulator battery, it will be necessary to connect a resistor with the appropriate resistance in series, which will limit the current flowing from the galvanic source. The values of this current will depend on the previously designed power pack as well as the parameters set in BMS, the exceeding of which will cut off the power source. A resistor limiting the charging current (fig. 6) will be necessary when applying power to the capacitors — after the packages are turned off by BCM or after service work. The value of the resistor is best selected by experimenting, and the calculated values included in tab. 8 should be used as the reference point. The current threshold above BMS is 110% of the rated current  $I_n$ , adequate to the nominal power of the drive.

Tab. 8. The value of supercapacitor charging resistor matched to the current efficiency of chemical cells, below the BMS protection threshold (own studies and calculations P. Chrabąszcz)

<b>Resistor limiting the capacitor charging current at maximum voltage (42V)</b>			
<b>Nominal current <math>I_n</math> [A]</b>	<b>110% <math>I_n</math> [A]</b>	<b><math>R=U/I</math> [<math>\Omega</math>]</b>	<b>Resistor strength [W]</b>
40	44	0.955	1628
80	88	0.477	3256
160	176	0.239	6512

Based on the sample catalogue data of individual cells [7], tab. 9. contains a summary of useful parameters for supercapacitors after battery assembly.

Tab. 9. List of parameters of considered supercapacitors individually and after assembling into a battery [7] (own studies and calculations P. Chrabąszcz)

Capacitor type	bcap1200	bcap1500	bcap2000	bcap3000
Capacity [F]	1200	1500	2000	3000
Nominal voltage [V]	2.7	2.7	2.7	2.7
maximum current [A]	930	1150	1500	1900
Single cell weight [g]	260	280	360	510
Single cell volume [cm <sup>3</sup> ]	272.7	313.2	375.8	508.5
ESR [mΩ]	0.58	0.47	0.35	0.29
The number of capacitors to obtain 42V [pcs]	16	16	16	16
Package Capacity 43.2V [F]	75	93.75	125	187.5
ESR 16S [Ω]	0.0093	0.0075	0.0056	0.0046
Package load 14S Q = C*U [C]	2775	3469	4625	6938
Package Weight 16S [g]	4160	4480	5760	8160
Package Volume 16S [cm <sup>3</sup> ]	4362.5	5011	6013	8135

## PROTOTYPE POWER APPLICATION PROSPECTS

Further considerations should include the requirements of dimensions, weight and operational conditions of the hybrid power source. The concentration of a large number of galvanic cells in combination with supercapacitors located in a small space of the device carries some risks. A large number of batteries with a certain efficiency, and therefore specific energy losses during charging and discharging may be the reason for raising the temperature in the power supply range above the permissible for the work of given cells, which can have dangerous consequences. In addition, a power source failure (spontaneous short circuit or even a small flooding with water) consisting of several dozen to a thousand galvanic cells with highly reactive and combustible lithium, supported by supercapacitors capable of generating a short-circuit current of a thousand amperes, may result in a fire, explosion causing injuries to personnel and losses in the environment.

## REFERENCES

- [1] Ciurys M., Dudzikowski I., *Analiza bezszczotkowego silnika prądu stałego z magnesami NdFeB*, 'Maszyny Elektryczne — Zeszyty Problemowe', 2011, No. 93, pp. 143–147 [Analysis of a brushless DC motor with NdFeB magnets — available in Polish].

- [2] Glinka T., *Maszyny elektryczne wzbudzone magnesami trwałymi*, WNT, Warszawa 2018 [*Electrical machines excited by permanent magnets* — available in Polish].
- [3] Hubik V., Toman J., Singule V., *BLDC motor control design in Matlab/Simulink*, 'Maszyny Elektryczne — Zeszyty Problemowe', 2010, No. 88, pp. 35–39.
- [4] Krykowski K., *Silniki PM BLDC — właściwości, sterowanie, aplikacje*, Publ. BTC, Legionowo 2015 [*PM BLDC motors — properties, control, applications* — available in Polish].
- [5] Popenda A., *Modelling of multiphase BLDC motor*, 'Przegląd Elektrotechniczny', 2018, Vol. 94, No. 1, pp. 85–88.
- [6] Zajkowski K., Duer S., *Diagnostyka silnika BLDC i układu sterowania*, 'Autobusy', 2012, No. 5, pp. 530–536 [*BLDC motor and control system diagnostics* — available in Polish].
- [7] *K2 ULTRACAPACITORS — 2.7V SERIES*, [online], [https://www.maxwell.com/images/documents/k2series\\_ds\\_10153704.pdf](https://www.maxwell.com/images/documents/k2series_ds_10153704.pdf) [access 02.04.2020].
- [8] *Samsung 26A 18650 Battery*, [online], <http://www.batteryonestop.com/baotongusa/products/datasheets/li-ion/Samsung-SDI-ICR18650-26A.pdf> [access 02.04.2020].
- [9] *Specifications for NCR18650GA*, [online], <https://www.orbtronic.com/content/Datasheet-specs-Sanyo-Panasonic-NCR18650GA-3500mah.pdf> [access 02.04.2020].

## KONCEPCJA MODELU NAPĘDU Z SILNIKIEM BLDC UWZGLĘDNIAJĄCEGO MODEL BATERYJNEGO OGNIWA ZASILAJĄCEGO

### STRESZCZENIE

Artykuł przedstawia koncepcję całościowego modelu napędu z silnikiem BLDC. Prototyp docelowy będzie uwzględniał w pełni funkcjonalny model ogniwa bateryjnego stanowiącego popularne źródło zasilania dla napędów z silnikami BLDC. W pracy zawarto dotychczasowe osiągnięcia w postaci funkcjonalnego modelu silnika BLDC wraz z wynikami badań symulacyjnych. Stanowią one wyniki cząstkowe, które miały na celu weryfikację poprawności opracowanego modelu silnika BLDC jako podstawy do dalszej rozbudowy. W artykule przedstawiono zasady doboru źródła zasilania dla prawidłowego określenia parametrów technicznych modelowanego ogniwa.

#### Słowa kluczowe:

napęd z silnikiem BLDC, napędy elektryczne, maszyny elektryczne, hybrydowe źródło zasilania, akumulatory li-ion, superkondensatory.

---

#### Article history

Received: 03.04.2020  
Reviewed: 02.05.2020  
Revised: 13.05.2020  
Accepted: 05.06.2020